LOW TEMPERATURE MODELING OF $I-V$ CHARACTERISTICS AND RF SMALL SIGNAL PARAMETERS OF SIGE HBTS

Except where reference is made to the work of others, the work described in this thesis is my own or was done in collaboration with my advisory committee. This thesis does not include proprietary or classified information.

Ziyan Xu

Certificate of Approval:

Fa Foster Dai
Professor
Electrical and Computer Engineering

Guofu Niu, Chair
Alumni Professor
Electrical and Computer Engineering

Vishwani Agrawal
James J. Danaher Professor
Electrical and Computer Engineering

George T. Flowers
Dean
Graduate School

Low Temperature Modeling of $I-V$ Characteristics and RF Small Signal Parameters of SiGe HBTs

Ziyan Xu

A Thesis

Submitted to

the Graduate Faculty of

Auburn University

in Partial Fulfillment of the

Requirements for the

Degree of

Master of Science

Auburn, Alabama
December 18, 2009

LOW TEMPERATURE MODELING OF $I-V$ CHARACTERISTICS AND RF SMALL SIGNAL PARAMETERS OF SIGE HBTS

Ziyan Xu

Permission is granted to Auburn University to make copies of this thesis at its discretion, upon the request of individuals or institutions and at their expense. The author reserves all publication rights.

_____

Signature of Author

_____

Date of Graduation

VITA

Ziyan Xu, daughter of Wenzhen Li and Jian Xu, was born on November 13, 1984, in Qingdao, P.R. China. She completed her high school degree from No.2 Qingdao High School in 2003. She received her bachelor degree from Hefei University of Technology in 2007, majoring in microelectronics. After that she was accepted into the electrical and computer engineering department in Auburn University in the fall of 2007, pursuing her master's degree.

Thesis Abstract

Low Temperature Modeling of $I-V$ Characteristics and RF Small Signal Parameters of SiGe HBTs

Ziyan Xu

Master of Science, December 18, 2009
(B.S., Hefei University of Technology, 2007)

84 Typed Pages

Directed by Guofu Niu

SiGe HBT has been attached great attention recently to be used for space exploration due to its high-quality performance compared with conventional Si bipolar transistor over an extremely wide temperature range. The currently used compact models fail to correctly function at very low temperature. This work investigates low temperature modeling of $I-V$ characteristics and RF small signal parameters of SiGe HBTs. Compact model Mextram is used as the starting point. A brief introduction of Mextram model is made. Both main current and base current modeling and their temperature scaling in Mextram model are reviewed.

New temperature scalable model of main current and base current is proposed and demonstrated with experimental data from 393 to 43 K. The temperature dependent ideality factor is proved necessary to model the low temperature current-voltage characteristics deviation from Shockley theory prediction. The relation $\triangle V_{BE} = kT/q \ln(J_{C1}/J_{C2})$, which is widely used in bandgap references (BGR) circuits, is shown no longer valid at low temperature.

The effect of tunneling on low temperature forward operation current is examined. Trap-assisted tunneling (TAT) current dominates the forward non-ideal base current. The way to distinguish tunneling current and main base current from forward gummel base current measurement is shown. A tunneling current model is developed to fit the lower bias region of forward base current from 110 to 43 K.

Small signal model is used to extract device small signal parameters. A two-step hot-after-cold optimization procedure is successfully used to fit Y-parameters from 1 to 35 GHz. The temperature dependence of important equivalent circuit parameters and implication on cryogenic RF circuit are examined.

ACKNOWLEDGMENTS

My deepest gratitude goes first and foremost to Dr. Guofu Niu, my supervisor, for his constant encouragement and guidance. I would like also to thank the other members of my committee, Dr. Fa Dai, and Dr. Vishwani Agrawal for their assistance.

Many thanks also go to Xiaoyun Wei, Lan Luo and Tong Zhang, my groupmates. I feel so lucky to study and work with them.

This thesis could not have been possible without the financial assistance of NASA and collaboration with Prof. John Cressler's SiGe group at Georgia Tech.

At last, I would like to thank my parents and families for their self-less support, understanding and love.

Style manual or journal used Journal of Approximation Theory (together with the style known as "aums"). Bibliography follows van Leunen's *A Handbook for Scholars*.

Computer software used The document preparation package TEX (specifically LATEX) together with the departmental style-file `aums.sty`.

TABLE OF CONTENTS

LIST OF FIGURES xi

1 INTRODUCTION 1
1.1 Cryogenic Operation of SiGe HBTs . . . 1
1.2 Thesis Contribution . . . 4

2 INTRODUCTION TO MEXTRAM 6
2.1 Main Current Modeling . . . 9
2.2 Base Current Modeling . . . 14
2.2.1 Linear Forward Base Current . . . 14
2.2.2 Non-Ideal Region . . . 14
2.3 Temperature Scaling . . . 14
2.3.1 Saturation Current I_S Temperature Scaling . . . 15
2.3.2 Base Saturation Current Temperature Scaling . . . 16
2.4 IC-CAP Built-in Mextram Model and Verilog-A Based Mextram . . . 16

3 IMPROVED MAIN CURRENT MODELING 19
3.1 $I_C - V_{BE}$ Modeling . . . 19
3.1.1 Improved N_F Temperature Scaling . . . 21
3.1.2 Improved I_S Temperature Scaling . . . 24
3.1.3 Summary . . . 27
3.2 N_F's Effect in Base Diffusion Charge . . . 29

4 BGR IMPLICATION 30
4.1 $V_{BE} - T$ . . . 30
4.2 $\Delta V_{BE} - T$ . . . 30
4.3 $V_{ref} - T$ . . . 31

5 BASE CURRENT MODELING 35
5.1 Trap-Assisted Tunneling Effect . . . 35
5.2 Separation of Main and Tunneling Base Current . . . 37
5.3 Ideality Factor, Saturation Current and Current Gain . . . 38
5.4 Tunneling Base Current Modeling . . . 41
5.5 Moderate Bias Region . . . 45
5.6 Summary . . . 48

6 SMALL SIGNAL MODELING 49
6.1 Equivalent Circuit . . . 49
6.2 Parameter Extraction . . . 50
6.2.1 Procedure . . . 50
6.2.2 Result . . . 53
6.3 Substrate Network Implementation . . . 59

7 CONCLUSION 62

BIBLIOGRAPHY 64

APPENDICES 67

A VERILOG-A CODE IMPLEMENTATION WITH KEY IMPROVED MODELS 68
A.1 Improved Ideality Factor Temperature Mapping . . . 68
A.2 Improved Saturation Current Temperature Mapping . . . 69
A.3 Modified Trasfer Current Model . . . 70
A.4 Modified Base Current Model . . . 71

LIST OF FIGURES

1.1 Energy band diagram of a graded-base SiGe HBT. [1] 2

1.2 Calculated base transit time using Philips mobility model and incomplete ionization model. 3

2.1 Equivalent Circuit of Mextram Level 504.7. [2] 8

2.2 Comparison collector current between IC-CAP built-in Mextram Model and Verilog-A implementation. 17

2.3 Comparison base current between IC-CAP built-in Mextram Model and Verilog-A implementation. 18

3.1 (a) Measured I_C versus V_{BE} at temperature from 43 to 393 K. (b) Extracted slope at each temperature compared with ideal $1/V_T$. (c) Extracted I_S at each temperature and $I_{S,T}$ Fitting from Mextram $I_{S,T}$ 20

3.2 The slope of I_C-V_{BE} from device simulation 21

3.3 N_F extracted from measurement versus N_F T-scaling models referenced to T_{nom}=300K. 22

3.4 Simulated versus measured $I_C - V_{BE}$. Extracted N_F are included. 23

3.5 Simulated versus measured $I_C - V_{BE}$. Extracted N_F and Thurmond's $E_{g,T}$ included. 26

3.6 I_S extracted from measurement versus I_S from the three models listed in Table 3.1 over 43-400 K. 27

3.7 (a) Simulated versus measured I_C-V_{BE} at high temperatures. (b) Simulated versus measured I_C-V_{BE} at low temperatures. 28

4.1 (a) Simulated versus measured V_{BE}-T dependence at I_0=0.1μA, 1μA, and 10μA. (b) Deviation of simulated V_{BE} from measured V_{BE} normalized by thermal voltage. 31

4.2 Wildar bandgap reference circuit. 32

4.3 (a) Simulated versus measured $\Delta V_{BE} - T$ at I_0=0.1μA, 1μA, and 10μA. (b) Deviation of simulated ΔV_{BE} from measured ΔV_{BE} normalized by thermal voltage. . . 33

4.4 (a) Simulated V_{REF} versus measured V_{REF} for three models. (b) Deviation of simulated V_{REF} from measured V_{REF} with respect to thermal voltage. 34

5.1 Illustration of trap-assisted tunneling in forward biased EB junction. 36

5.2 Forward and reverse gummel measurement data: (a) forward gummel I_C-V_{BE}, (b) forward gummel I_B-V_{BE}, (c) reverse gummel I_E-V_{BC} and (d) reverse gummel I_B-V_{BC}. 37

5.3 Difference between linear fitting with and without iteration at 43 K. 38

5.4 Comparison of ideality factor and saturation current between including and excluding TAT current: (a) $I_{S,BE}$-T, (b)N_{EI}-T, (c) I_S-T, (d)N_F-T. 39

5.5 Comparison of ideality factor and saturation current between collector and base: (a) saturation current, (b)ideality factor. 40

5.6 The slopes of (a) $I_C - V_{BE}$ and (b) extracted from simulation and measurement from 43 to 300 K. 41

5.7 Comparison between current gain obtained by (a) total I_C/I_B and (b)excluding tunneling current and current gain obtained at $I_C = 10^{-5}$ A (c) by (a) and (b). . . . 42

5.8 (a) Base tunneling current at 43, 60 76, 93 and 110 K; (b) The extracted ideality factor is proportional to $1/T$; (C) $S = N_{E,TAT} \times V_T$. 43

5.9 The temperature scaling of tunneling saturation current at 43, 60, 76, 93 and 110 K. 46

5.10 Comparison between measurement an modeling results for 43 to 110 K: (a) combined with ideal base fitting, (b) TAT current modeling 47

5.11 Measured and modeled I_B-V_{BE} from 43-93 K. 48

6.1 Small-signal equivalent circuit used for SiGe HBTs. 50

6.2 Small-signal equivalent circuit used for cold state. 51

6.3 Measured f_T-I_C as a function of V_{CB} at various temperatures. 51

6.4 Selected I_C points for each temperature extraction 52

6.5 Measured and simulated Y-parameters at 300 K. 54

6.6 Measured and simulated Y-parameters at 223 K. 54

6.7 Measured and simulated Y-parameters at 162 K. 55

6.8 Measured and simulated Y-parameters at 93 K. 55

6.9 Extracted g_m-I_C results compared with ideal I_C/V_T with and without self-heating at 300, 223, 162 and 93 K. 56

6.10 Extracted C_π-I_C at 300, 223, 162 and 93 K. 57

6.11 Extracted C_{bci}-I_C and C_{bcx}-I_C at 300, 223, 162 and 93 K. 58

6.12 Extracted total $C_{BC}(C_{bci} + C_{bcx})$ vs V_{BE} from cold and hot extraction. 58

6.13 Extracted R_{bi} at $I_C = 1$ mA and R_s vs T. 59

6.14 Small-signal equivalent circuit for substrate network. 60

6.15 Small-signal equivalent circuit for substrate network. 61

7.1 Modified equivalent circuit. 63

CHAPTER 1

INTRODUCTION

After being studied and developed for years, Silicon- Germanium (SiGe) technology has pervasively used in personal communications devices and military products. The heart of SiGe technology is a SiGe heterojunction bipolar transistor (HBT), which has a high compatibility with BiCMOS technology, is easy to integrated with existing BiCMOS device [3]. The bandgap engineering by introducing SiGe alloy into the base upgrades both DC and AC performance of conventional Si bipolar transistor (BJT). The Ge-grading induced extra drift field in the neutral bases shown in Fig. 1.1 increases the collector current density (J_C) through increasing electron injection at emitter-base (EB) junction, yielding higher current gain. This induced field also accelerates the minority carrier transportation, shortens the transit time across the base and increases the frequency response [3].

1.1 Cryogenic Operation of SiGe HBTs

The low temperature performance of SiGe HBTs has been investigated for many years [4]. As the bipolar transistor is a minority carrier device, which obeys the Shockley boundary conditions, n_{i0}^2 is proportional to the exponential of the bandgap. Intuitively, the change in bandgap due to Ge-grading will associate with exponential change in current. Moreover, these change will be naturally exaggerated by thermal voltage V_T with cooling. With a glance of the device's temperature mapping equations, we are able to find that both DC and AC characteristic of SiGe HBTs are favorably affected by cooling. The term V_T is unavoidably functioning almost everywhere [5].

A good example of SiGe HBTs advantage over Si BJTs is that the induced field offers a method to offset the inherent τ_b associated with cooling, yielding an f_T improving with cooling [5].

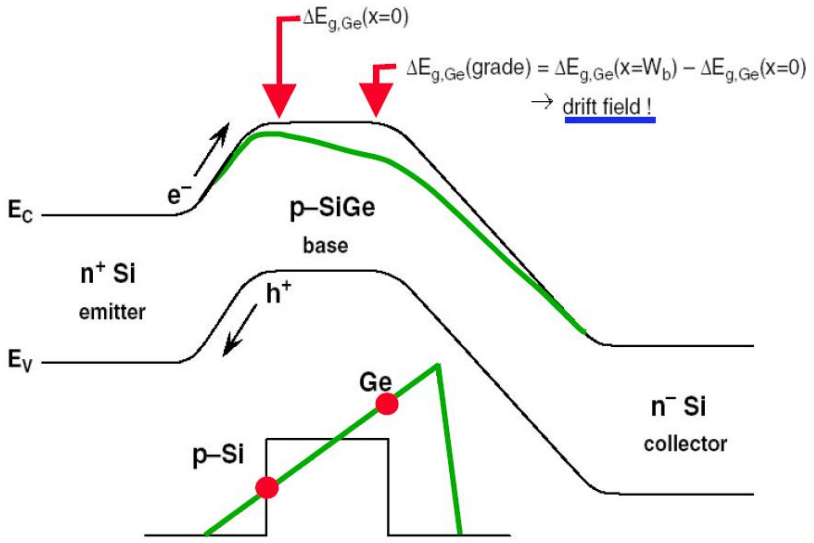

Figure 1.1: Energy band diagram of a graded-base SiGe HBT. [1]

In (1.1) and (1.2), the base transit time $\tau_{b,Si}$ of Si and $\tau_{b,SiGe}$ of SiGe are given respectively [3].

$$\tau_{b,Si} = \frac{W_b^2}{2D_{nb}}; \tag{1.1}$$

$$\tau_{b,SiGe} = \frac{W_b^2}{D_{nb}} \frac{kT}{\triangle E_{g,Ge}(grade)} \cdot \left\{ 1 - \frac{kT}{\triangle E_{g,Ge}(grade)} \left[1 - \exp(-\triangle E_{g,Ge}(grade) / kT \right] \right\}. \tag{1.2}$$

Based on a theoretical calculation, the comparison between Si and SiGe base transit time is shown in Fig. 1.2. For simplicity, the base of SiGe HBT is assumed to be 50 nm wide with uniform doping of 10^{18}cm^{-3} and a total bandgap grading of 100 meV. The Philips unified mobility model [6] is used , while incomplete ionization mobility model reported in [7] is used to model freeze-out by affecting diffusivity. Whatever the freeze-out is taken into consideration or not, the transit time of SiGe HBT is much smaller than that of Si BJT. This clearly illustrates the advantages of SiGe HBT in low temperature operation.

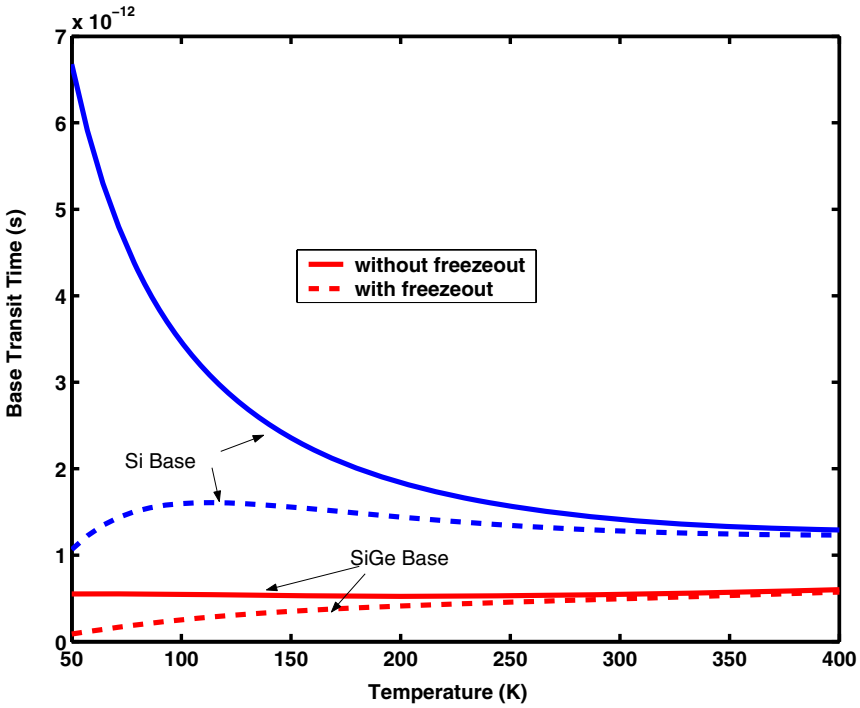

Figure 1.2: Calculated base transit time using Philips mobility model and incomplete ionization model.

Due to the excellent analog and RF performance of SiGe HBTs over an extremely wide range of temperatures, together with its built-in total dose radiation tolerance [5], SiGe BiCMOS technology is currently being used to develop electronics for space applications. For instance, SiGe BiCMOS electronic components can operate directly in the extreme ambient environment found on the lunar surface, where temperatures cycle from -180 °C to +125 °C (a 300 °C swing over 28 days) and radiation exposure exists (both total dose and single event effects). Operating electronic systems under ambient conditions, without excessive shielding or by providing heaters inside Warm Electronics Boxes (WEBs) to protect electronics from their surroundings (current practice), can save substantial size, weight, and power, increasing the reliability and decreasing the cost for these missions [8]. The device modeling of high accuracy and convergence is the prerequisite. This is the basic motivation for cryogenic temperature modeling.

1.2 Thesis Contribution

In this work, Mextram model is used as a starting point and introduced in Chapter 2. The exquisite model is advanced in modeling quasi-saturation, Kirk effect, impact ionization and so on. It is limited, however, in describing the cryogenic behavior of transistors.

Next in Chapter 3, an improved model of DC main current is proposed after examination of existing models. It is found that q_B factor is far from enough to produce the slope in medium $I_C - V_{BE}$ region [9]. The existing I_S T-scaling model does not work below 200 K. The T dependent ideality factor must be included into both $I_C - V_{BE}$ equation and I_S T-scaling equation.

The same strategy is used to model ideal base current. At cryogenic temperatures, the trap-assisted tunneling dominates non-ideal base current at forward operation. However, the compact models, which may have described the tunneling current at reverse operation, never include the trap-assisted tunneling current. In this work, the trap-assisted tunneling effect is examined and is added to model base current. The iteration method is used to distinguish ideal base current and the trap-assisted tunneling current. T-scaling of the tunneling saturation current is also proposed.

The temperature dependence of $I_C - V_{BE}$ is very important for designing bandgap references where the negative temperature coefficient of V_{BE} is neutralized by the positive temperature coefficient of ΔV_{BE} of two transistors operating at different current densities [10]. $\Delta V_{BE} = kT/q \ln(J_{C1}/J_{C2})$ in existing models and is linearly proportional to absolute temperature T. In Chapter 5, this relation is shown invalid at low temperature. Significantly better fitting of $V_{BE} - T$, and $\Delta V_{BE} - T$ characteristics are obtained by including T-scaling of N_F into this relation.

In Chapter 6, the small signal modeling is examined. Parameter extraction strategy and fitting results of Y-parameter over temperature are presented and discussed. Simulation results from 1 to 35 GHz of a first-generation SiGe HBT with a 50 GHz peak f_T at 300 K are presented in the temperature range of 393 K to 93 K.

All modification is made in Mextram Verilog-A code. However, the $I - V$ model can be used in other compact models too, as all of the models have similar main current base current equations.

CHAPTER 2

INTRODUCTION TO MEXTRAM

Mextram model is a widely used vertical bipolar transistor model. Mextram is the acronym of the "most exquisite transistor model". The first Mextram release was introduced as Level 501 in 1985 [11]. Later Level 502, 503 and 504 were respectively released in 1987 [12], 1994 and 2000 [13]. And development was never stopped following the requirement of updated technology. The latest accessible version is Level 504.7 [2].

Following effects descriptions are contained in Mextram according to its latest release Level 504.7 [2]:

1. Bias-dependent Early effect
2. Low-level non-ideal base currents
3. High-injection effects
4. Ohmic resistance of the epilayer
5. Velocity saturation effects on the resistance of the epilayer
6. Hard and quasi-saturation (including Kirk effect)
7. Weak avalanche (optionally including snap-back behaviour)
8. Charge storage effects
9. Split base-collector and base-emitter depletion capacitance
10. Substrate effects and parasitic PNP
11. Explicit modeling of inactive regions
12. Current crowding and conductivity modulation of the base resistance
13. First order approximation of distributed high frequency effects in the intrinsic base (high-frequency current crowding and excess phase-shift)
14. Recombination in the base (meant for SiGe transistors)
15. Early effect in the case of a graded bandgap (meant for SiGe transistor)

16. Temperature scaling

17. Self-heating

18. Thermal noise, shot noise and 1/f-noise

In Mextram model, there are five internal nodes and 79 parameters, including parameters of model flag, parameters of noise and the reference temperature, parameters of temperature scaling, parameters of individual transistor design and parameters to be determined by the fitting the model to the transistor characteristics of a specific device and at a specific temperature.

Some parts of the model are optional and can be switched on or off by setting flags. These are the extended modeling of reverse behaviour, the distributed high-frequency effects, and the increase of the avalanche current when the current density in the epilayer exceeds the doping level.

The governing Mextram equations are formulated having in mind NPN transistors, but the model can be equally well used for PNP transistors by simple change of the current and charge polarity. Besides, both three-terminal devices (discrete transistor) and four-terminal devices (IC-processes which also have a substrate) can be described.

Fig. 2.1 shows the equivalent circuit of Mextram model as it is specified in its latest release Level 504.7 [2]. The branches representing model currents and charges are schematically associated with different physical regions of a bipolar transistor separated by the base-emitter, base-collector, and substrate-collector junctions. All current and charge branches in Mextram are given as explicit functions of external and internal nodal potentials and there are no implicit modeling variables that require internal iterations [11].

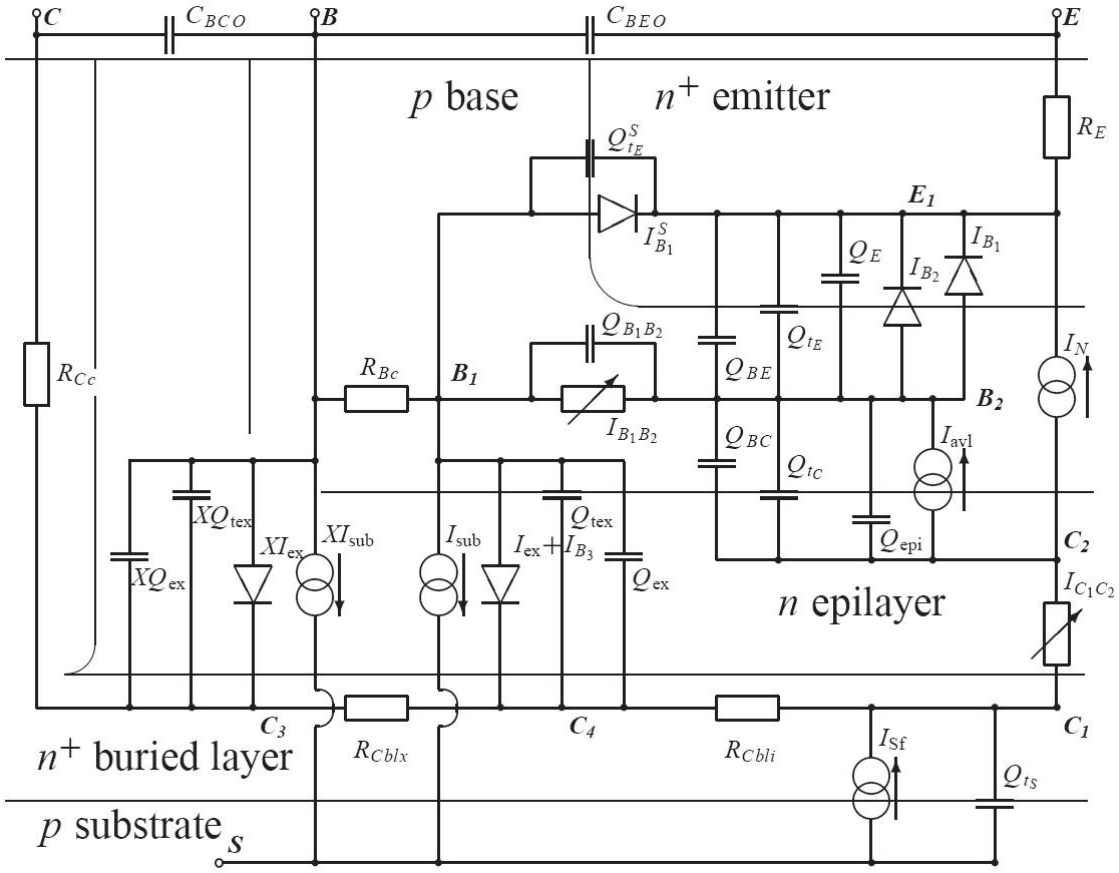

Figure 2.1: Equivalent Circuit of Mextram Level 504.7. [2]

2.1 Main Current Modeling

In Mextram, the integral charge control relation (ICCR) is used for the description of the main current, which is I_N in Fig. 2.1. Following repeats the brief derivation of this relation. Most of the derivations are on the reference of [2].

The electron density in the base region can be written as

$$J_n = n\mu_n \frac{dE_{fn}}{dx}, \tag{2.1}$$

in which n is electron concentration, μ_n is the electron minority carrier mobility. The difference between quasi-Fermi level is

$$E_{fn} - E_{fp} = kT \ln\left(\frac{np}{n_i^2}\right), \tag{2.2}$$

where k is Boltzmann's constant and n_i is the effective intrinsic concentration. As the hole is majority in the base, $\frac{dE_{fp}}{dx}$ is assumed to be zero. Thus.

$$J_n = n\mu_n \frac{d\left(E_{fn} - E_{fp}\right)}{dx} = qD_n \frac{n_i^2}{p} \frac{d}{dx}\left(\frac{np}{n_i^2}\right), \tag{2.3}$$

where D_n is the electron diffusivity, equal to $\mu_n kT/q$. Moving $qD_n\frac{n_i^2}{p}$ to the left side gives

$$\frac{J_n p\,(x)}{qD_n n_i^2} dx = d\left(\frac{np}{n_i^2}\right). \tag{2.4}$$

Integrating on both sides gives

$$J_n \int_{x_{E1}}^{x_{C2}} \frac{p\,(x)}{qD_n n_i^2} dx = \exp\left(\frac{V_{B_2C_2}}{V_T}\right) - \exp\left(\frac{V_{B_2E_1}}{V_T}\right), \tag{2.5}$$

$$J_n = -\frac{q^2 D_n n_i^2}{Q_B}\left[\exp\left(\frac{V_{B_2E_1}}{V_T}\right) - \exp\left(\frac{V_{B_2C_2}}{V_T}\right)\right], \tag{2.6}$$

and

$$Q_B = qA_{em} \int_{X_{E_1}}^{x_{C_2}} p\,(x)\,dx. \tag{2.7}$$

X_{E_1} and X_{C_2} are the positions of the internal emitter node and internal collector node defined in Mextram. Both of them can be considered at the actual junctions. Since the direction from emitter to collector is taken as positive $x-$ direction, and the current density is negative for the forward mode of operation,

$$I_N = -A_{em} J_n, \tag{2.8}$$

where A_em is effective emitter area. And the main current becomes

$$I_N = \frac{q^2 D_n n_i^2 A_{em}^2}{Q_B} \left[\exp\left(\frac{V_{B_2E_1}}{V_T} \right) - \exp\left(\frac{V_{B_2C_2}}{V_T} \right) \right]. \tag{2.9}$$

In Mextram, the main current based on the ICCR relation is given by

$$I_f = I_S \exp\left(\frac{V_{B_2E_1}}{V_T} \right), \tag{2.10}$$

$$I_r = I_S \exp\left(\frac{V_{B_2C_2}}{V_T} \right), \tag{2.11}$$

$$I_N = \frac{I_f - I_r}{q_B}. \tag{2.12}$$

Here, the base charge Q_B normalized to the base charge at zero bias Q_{B0} is denoted by q_B. Hence,

$$I_S = \frac{q^2 D_n A_{em}^2 n_i^2}{Q_{B0}}, \tag{2.13}$$

and

$$Q_B = Q_{B0} + Q_{tE} + Q_{tC} + Q_{BE} + Q_{BC}. \tag{2.14}$$

For low injection, Q_B is the sum of the base charge at zero bias Q_{B0}, and the extra charge Q_{tE} and Q_{tC} due to the change in emitter side and collector side depletion region width. Q_{BE} is diffusion charge related to forward operation and depends on the base-emitter bias; Q_{BC} is diffusion charge related to reverse operation and depends on the base-collector bias.

Firstly the diffusion charge is neglected for the moment, so the normalized base charge becomes

$$q_0 = \frac{Q_B}{Q_{B0}} = 1 + \frac{Q_{tE}}{Q_{B0}} + \frac{Q_{tC}}{Q_{B0}}. \tag{2.15}$$

Define that

$$V_{tE} = \frac{Q_{tE}}{\left(1 - XC_{jE}\right) C_{jE}}, \tag{2.16}$$

and

$$V_{tC} = \frac{Q_{tC}}{XC_{jC}C_{jC}}, \tag{2.17}$$

so

$$q_0 = 1 + \frac{V_{tE}}{V_{er}} + \frac{V_{tc}}{V_{ef}}. \tag{2.18}$$

V_{er} and V_{ef} are reverse and forward Early voltage. XC_{jE} is defined in Mextram the fraction of the emitter-base depletion capacitance that belongs to the sidewall. XC_{jC} is the fraction of the collector-base depletion capacitance under the emitter. Taking punch-through into the account, Mextram uses q_1 directly instead of q_0.

$$q_1 = \frac{1}{2}\left(q_0 + \sqrt{q_0^2 + 0.01}\right). \tag{2.19}$$

Next consider base diffusion charge only and neglect Early effect for the moment. The base doping profile in the electron density is assumed to be linear:

$$n(x) = n(0)\left(1 - \frac{x}{W_B}\right) + n(W_B)\left(\frac{x}{W_B}\right). \tag{2.20}$$

The total electron charge is

$$Q_{B,elec} = \frac{1}{2} q A_{em} W_B n(0) + \frac{1}{2} q A_{em} W_B n(W_B). \tag{2.21}$$

Define

$$Q_{BE} = \frac{1}{2} Q_{B0} n_0, \tag{2.22}$$

and

$$Q_{BC} = \frac{1}{2} Q_{B0} n_B. \tag{2.23}$$

They are respectively the charge contributed from the electron density at the base-emitter edge and at the base-collector edge. The base transit time is approximately constant, so

$$Q_{BE} = \tau_B I. \tag{2.24}$$

Combining with (2.9), the following equation can be got

$$I = \frac{I_S \exp\left(\frac{V_{B_2E_1}}{V_T}\right)}{1 + \frac{\tau_B I}{Q_{B0}}}. \tag{2.25}$$

Solving for I get

$$I = \frac{2 I_S \exp \frac{V_{B_2E_1}}{V_T}}{1 + \sqrt{1 + \frac{4 I_S}{I_K} \exp\left(\frac{V_{B_2E_1}}{V_T}\right)}}. \tag{2.26}$$

Define low current and high current

$$I_{low} = I_S \exp\left(\frac{V_{B_2E_1}}{V_T}\right), \tag{2.27}$$

$$I_{high} = \sqrt{I_S I_K} \exp\left(\frac{V_{B_2E_1}}{2V_T}\right). \tag{2.28}$$

Calculating the point where both asymptotes cross get

$$I_{low} = I_{high} \Longrightarrow I = I_K. \tag{2.29}$$

I_K is the so-called knee current.

$$n_0 = \frac{2Q_{BE}}{Q_{B0}} = \frac{2\tau_B I}{Q_{B0}} = \frac{2I}{I_K}, \tag{2.30}$$

so

$$f_1 = \frac{4I_S}{I_K} \exp\left(\frac{V_{B_2E_1}}{V_T}\right). \tag{2.31}$$

$$n_0 = \frac{f_1}{1 + \sqrt{1 + f_1}} \tag{2.32}$$

For reverse,

$$f_2 = \frac{4I_S}{I_K} \exp\left(\frac{V_{B_2C_2}}{V_T}\right). \tag{2.33}$$

$$n_B = \frac{f_2}{1 + \sqrt{1 + f_2}}. \tag{2.34}$$

Then combine early effect with base charge diffusion, we can get

$$Q_{BE} = \frac{1}{2} q_1 Q_{B0} n_0, \tag{2.35}$$

$$Q_{BC} = \frac{1}{2} q_1 Q_{B0} n_B, \tag{2.36}$$

$$q_B = q_1 \left(1 + \frac{1}{2} n_0 + \frac{1}{2} n_B\right). \tag{2.37}$$

2.2 Base Current Modeling

2.2.1 Linear Forward Base Current

In Mextram, the total ideal base current is separated into a bulk and a side-wall current. Both depend on separate voltages. β_f as a parameter that gives the ratio between the main saturation current and base saturation current. The equations are given as:

$$I_{B_1} = \left(1 - XI_{B_1}\right) \frac{I_S}{\beta_f} \left(\exp\left(\frac{V_{B_2E_1}}{V_T} \right) - 1 \right), \tag{2.38}$$

$$I_{B_1}^S = XI_{B_1} \frac{I_S}{\beta_f} \left(\exp\left(\frac{V_{B_1E_1}}{V_T} \right) - 1 \right). \tag{2.39}$$

XI_{B1} is the parameter defined in Mextram to express the part of ideal base current that belongs to sidewall.

2.2.2 Non-Ideal Region

The non-ideal forward base current is given by I_{B_2}

$$I_{B_2} = I_{B_f} \left(\exp\left(\frac{V_{B_2E_1}}{m_{LF}V_T} \right) - 1 \right), \tag{2.40}$$

and is simply a diode current with a non-ideality factor m_{Lf}.

2.3 Temperature Scaling

Following are the T-scaling equations defined in Mextram. T_{RK} is degree Kelvin at which the parameters are determined.

$$t_N = \frac{T_K}{T_{RK}}, \tag{2.41}$$

$$V_T = \left(\frac{k}{q} \right) T_K, \tag{2.42}$$

$$V_{T_R} = \left(\frac{k}{q}\right) T_{RK}, \tag{2.43}$$

$$\frac{1}{V_{\triangle T}} = \frac{1}{V_T} - \frac{1}{V_{T_R}}. \tag{2.44}$$

2.3.1 Saturation Current I_S Temperature Scaling

The T-scaling of saturation current is given as

$$I_{ST} = I_S t_N^{4-A_B-A_{QB0}+dA_{I_S}} \exp\left[\frac{-V_{gB}}{V_{\triangle T}}\right]. \tag{2.45}$$

Below is the derivation.

$$I_{S,T} = A_e m \frac{q^2 D_{n,T} n_{i,T}^2}{Q_{B0}}, \tag{2.46}$$

$$I_{S,T_{rK}} = A_e m \frac{q^2 D_{n,T_{rK}} n_{i,T_{rK}}^2}{Q_{B0}}. \tag{2.47}$$

As

$$D_n = \mu_n \frac{kT}{q}, \tag{2.48}$$

$$I_{S,T} = I_{S,T_{rK}} \frac{T}{T_{rK}} \frac{\mu_{n,T}}{\mu_{n,Tom}} \frac{n_{i,T}^2}{n_{i,T_{rK}}^2}. \tag{2.49}$$

Since

$$n_i^2 \propto T^3 \exp\left(-\frac{E_{g,T}}{kT}\right), \tag{2.50}$$

$$\mu_n \propto T^{-m}, \tag{2.51}$$

$$I_{S,T} = I_{S,T_{rk}} t_N^{(3-m)} \exp\left(-\frac{V_{g,T}}{V_T} + \frac{V_{g,T_{rK}}}{V_{T_{rK}}}\right), \tag{2.52}$$

$$-\frac{V_{g,T}}{V_T} + \frac{V_{g,T_{rK}}}{V_{T_{rK}}} = -\frac{1}{V_T}\left[V_{gB}\left(1 - t_N\right) - BT \ln t_N\right]. \tag{2.53}$$

Hence,

$$I_{ST} = I_S t_N^{4-m+B\frac{T_{rK}}{V_{T_{rK}}}} \exp\left[\frac{-V_{gB}}{V_{T_{rK}}}\left(1 - \frac{1}{t_N}\right)\right]. \tag{2.54}$$

which is equivalent to (2.45).

2.3.2 Base Saturation Current Temperature Scaling

For base current, the T-scaling of saturation current is modeled as

$$I_{BfT} = I_{Bf} t_N^{6-2m_{Lf}} \exp\left[\frac{-V_{gj}}{m_{Lf} V_{\triangle T}}\right], \tag{2.55}$$

and the current gain:

$$\beta_{fT} = \beta_f t_N^{(A_E - A_B - A_{Q_{B0}})} \exp\left[\frac{-dV_{g\beta f}}{V_{\triangle} T}\right]. \tag{2.56}$$

2.4 IC-CAP Built-in Mextram Model and Verilog-A Based Mextram

The analog hardware description language (AHDL) Verilog-A is high-level language developed to describe the structure and behavior of analog system and their components [14]. The capability of Verilog-A to handle state-of-the-art compact bipolar transistor modeling mixed with extra modeling has been demonstrated [15].

The Mextram Level 503 and 504 has been implemented by IC-CAP through work jointly carried out by Philips Research Labs, TU Delft, and Agilent EEsof EDA [16]. The IC-CAP built-in C-functions can be used for model parameter extraction [17].

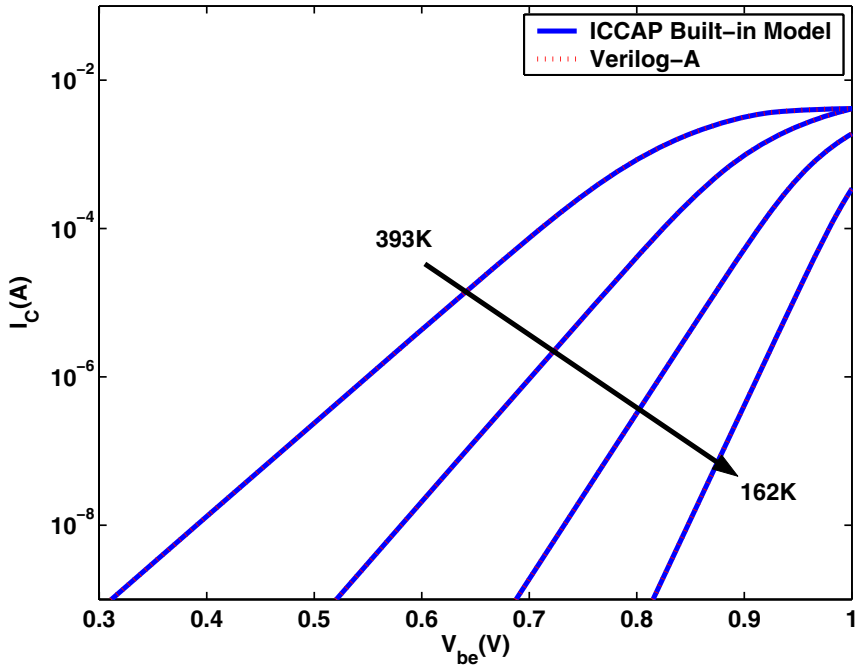

Figure 2.2: Comparison collector current between IC-CAP built-in Mextram Model and Verilog-A implementation.

Verilog-A code 504.7 is downloaded from Mextram website.We first need to make sure the Verilog-A code is "functional correct" by comparing with built-in model in IC-CAP. Forward Gummel simulation at 393, 300, 223 and 162 K are performed in both ways. The simulation results shown in Fig. 2.2 and Fig. 2.3 are highly consistent, which proves that Verilog-A code used is correct. Convergence problem at lower temperature is encountered using both Verilog-A code and the built-in model.

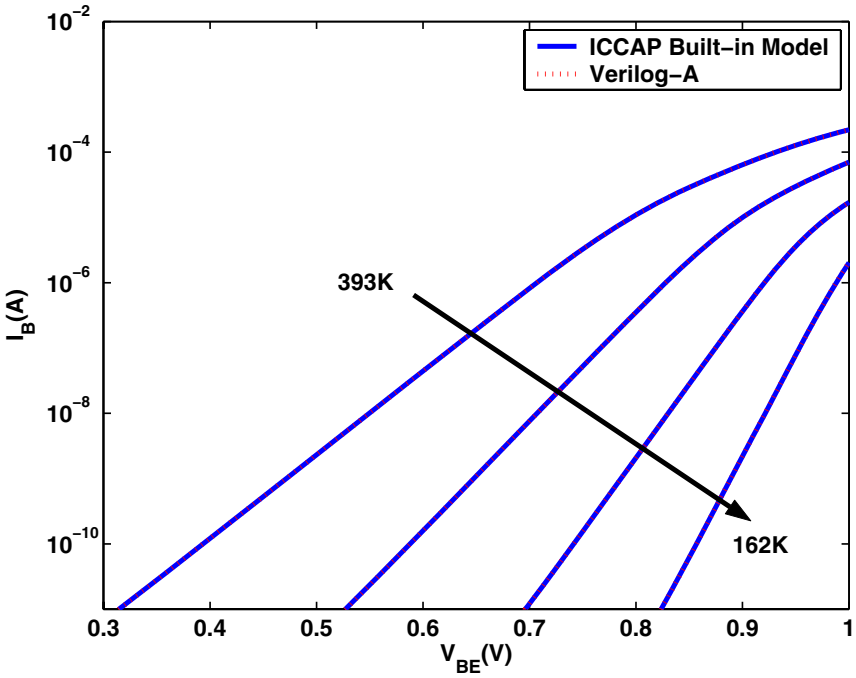

Figure 2.3: Comparison base current between IC-CAP built-in Mextram Model and Verilog-A implementation.

CHAPTER 3

IMPROVED MAIN CURRENT MODELING

Shockley theory predicts that $I_C - V_{BE}$ has an exponential relation in moderate injection region, so on a semilog scale the $I_C - V_{BE}$ slope is $1/V_T$. Below 100 K, however, we find that the T-dependence of $I_C - V_{BE}$ becomes increasingly weaker. Whereas in other compact models like Gummel-Poon and VBIC, ideality factor N_F is included [18] [19], though its value is almost unity constant, in Mextram the deviation of $I_C - V_{BE}$ from $1/V_T$ is modeled with q_B [17] as talked in Chapter 2, and it was believed that q_B is sufficient in modeling the slope of $I_C - V_{BE}$, and using ideality factor could complicate parameter extraction. In this chapter, only q_B factor is shown far from enough to reproduce the deviation and a method including T dependent ideality factor in both $I_C - V_{BE}$ equation and $I_S - T$ equation for modeling will be proposed compared with experimental results.

3.1 $I_C - V_{BE}$ Modeling

For clarity of discussion, we consider forward mode only where I_C relates to V_{BE} by [17] [18] [19]

$$I_C = \frac{1}{q_B} I_S \left(exp\left(\frac{V_{BE}}{N_F V_T} \right) - 1 \right). \tag{3.1}$$

Here q_B accounts for modulation of base charge (or effective charge for HBTs), I_S is the saturation current, and N_F is the ideality factor. $V_T = kT/q$. In Shockley's junction theory, N_F=1, and any deviation of I_C-V_{BE} in medium injection can only be modeled through q_B. This approach is taken by Mextram as it was believed to be more physical. In the SPICE Gummel-Poon (SGP) and VBIC models, N_F is used as a fitting parameter, and does not have a clear physical meaning.

As both q_B and N_F affect the slope of $I_C - V_{BE}$, as long as $I_C - V_{BE}$ is well fitted, both approaches can be used. It is found that, at low temperatures, the slope of measured $I_C - V_{BE}$,

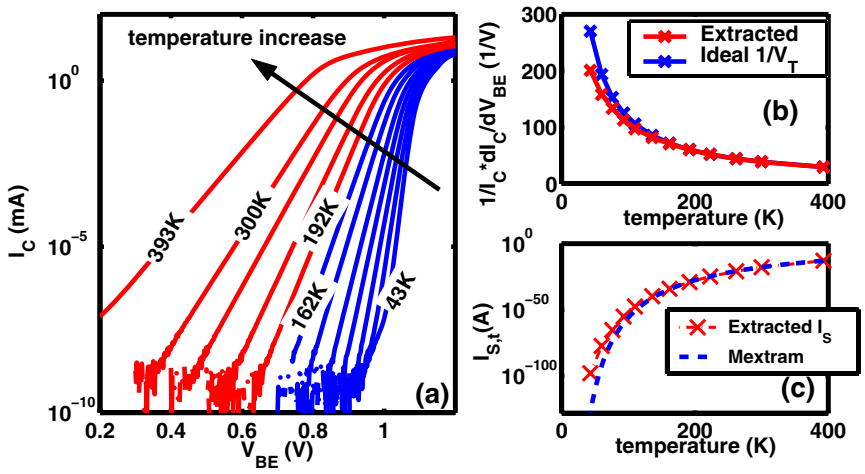

Figure 3.1: (a) Measured I_C versus V_{BE} at temperature from 43 to 393 K. (b) Extracted slope at each temperature compared with ideal $1/V_T$. (c) Extracted I_S at each temperature and $I_{S,T}$ Fitting from Mextram $I_{S,T}$.

shown in Fig. 3.1 (a), significantly deviates from the ideal $1/V_T$ value, which cannot possibly be reproduced using q_B, which is primarily due to reverse Early effect at medium injections where the $I_C - V_{BE}$ relation is linear on a semilog scale. To identify the physical reasons, we performed both drift-diffusion and hydrodynamic device simulation of the SiGe HBT used. The simulated $I_C - V_{BE}$ slope, however, shows a much less deviation from ideal value than what we observed in measurement. The results are shown in Fig. 3.2. As all of the higher order effects in compact models are naturally included in device simulation, we conclude that such a deviation is likely not caused by effects modeled by q_B, and is due to unknown physics to the best of our knowledge.

Given that existing q_B models fail to model $I_C - V_{BE}$ slope, the use of N_F becomes necessary. Our strategy is to use N_F as the main parameter for fitting the slope of $I_C - V_{BE}$ in the medium I_C range, where $I_C - V_{BE}$ is virtually linear on semilog scale, and use q_B for fine tuning. Furthermore, Fig. 3.1 (c) show I_S extracted versus temperature and Mextram modeling. The difference at low temperature the I_S T-scaling should be revaluated too.

As convergence problem is encountered when simulation runs at low temperature in Mextram and the high consistency in describing moderate $I_C - V_{BE}$ characteristics between VBIC and

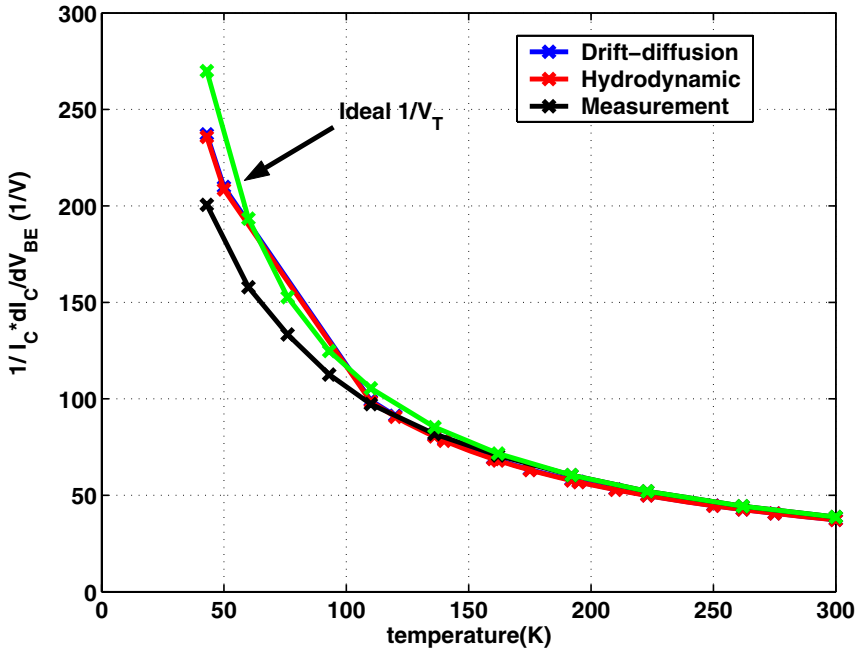

Figure 3.2: The slope of I_C-V_{BE} from device simulation .

Mextram, the evaluation below will be first preformed by VBIC using Verilog-A code, and then transferred to Mextram.

3.1.1 Improved N_F Temperature Scaling

Here, we propose a new nonlinear $N_{F,T}$ equation

$$N_{F,T} = N_{F,nom}\left(1 - \frac{T - T_{nom}}{T_{nom}}\left(A_{NF}\frac{T_{nom}}{T}\right)^{X_{NF}}\right). \tag{3.2}$$

The term *nom* means the reference temperature at which all parameters are determined. Fig. 3.3 plots the extracted N_F, a constant $N_{F,T}$, a linear $N_{F,T}$ and the $N_{F,T}$ from (3.2). (3.2) produces the best fitting and is used below.

By including extracted N_F into Verilog-A, however, the simulated $I_C - V_{BE}$ still cannot fit data below 192 K, as shown in Fig. 3.4. $I_C - V_{BE}$ slope is now correct though. The data clearly show that the main problem is that I_S (intercept with Y-axis) is underestimated by the $I_S - T$ model

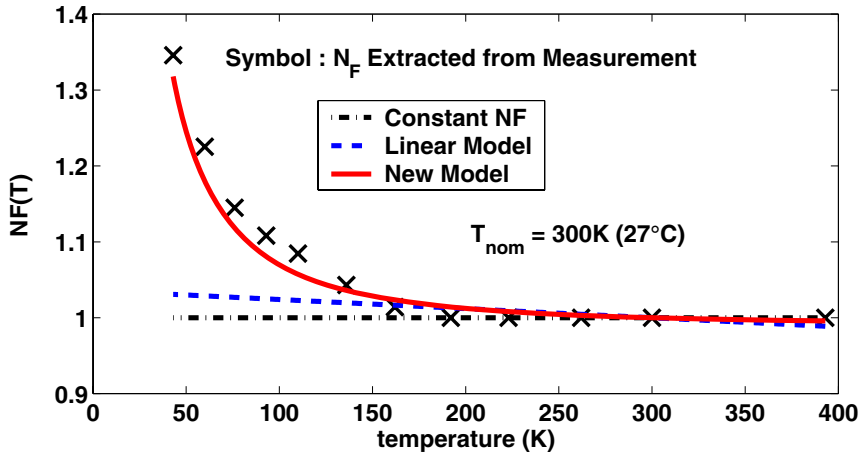

Figure 3.3: N_F extracted from measurement versus N_F T-scaling models referenced to T_{nom}=300K.

at lower temperatures. Therefore we need to develop a better $I_S - T$ model that gives higher I_S at lower T but does not change I_S at higher T.

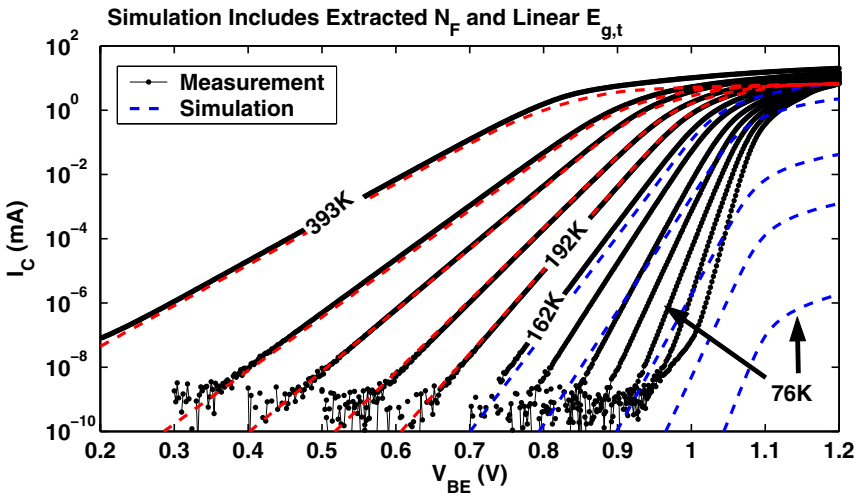

Figure 3.4: Simulated versus measured $I_C - V_{BE}$. Extracted N_F are included.

3.1.2 Improved I_S Temperature Scaling

In existing compact models, the I_S temperature dependence is described by

$$I_{S,T} = I_{S,nom}\left(\frac{T}{T_{nom}}\right)^{X_{IS}} \exp\left(\frac{-E_{a,nom}\left(1-\frac{T}{T_{nom}}\right)}{V_T}\right), \tag{3.3}$$

which has been derived in Chapter 2.

To increase I_S in lower temperatures, first comes the thought of bandgap. If a linear bandgap temperature scaling is used,

$$E_{g,T} = E_{g,0} - \alpha T, \tag{3.4}$$

$$E_{a,nom} = E_{g,0}, \tag{3.5}$$

$$X_{IS} = \gamma + 1 - m, \tag{3.6}$$

in which the value of γ is 3.

If Lin and Salama's bandgap temperature scaling is used,

$$E_{g,T} = E_{g,0} + AT - BT\ln T, \tag{3.7}$$

$$E_{a,nom} = E_{g,0}, \tag{3.8}$$

$$X_{IS} = \gamma + 1 - m + B\frac{T_{nom}}{V_{T_{nom}}}. \tag{3.9}$$

In fact, for Lin and Salama's method, part of nonlinear coefficient of Eg,t is lumped into the X_{IS} term, as proved in [20] . The value of X_{IS} needs to be adjusted.

But during parameter extraction, both X_{IS} and E_a are fitting parameter, inevitably, we can only get their value to achieve the optimized fitting result, and are not able to tell which bandgap t-scaling is used. That is, the failure of fitting shown in Fig. 3.4 at low temperature is not caused by linear bandgap t-scaling.

Next we extend the above T-scaling equation for the classical Thurmond bandgap T-scaling model, $E_{g,T} = E_{g,0} - \alpha T^2/(T+\beta)$ [21]. α and β are fitting parameters. A lengthy but straightforward derivation leads to a new $I_{S,T}$ T-scaling equation that can be written in the same form as (3.3), but with a T-dependent E_a [22].

$$E_{a,T} = E_{g,0} + \frac{\alpha\beta T T_{nom}}{(T+\beta)(T_{nom}+\beta)}. \tag{3.10}$$

The activation energy at $T = T_{nom}$, denoted as $E_{a,nom}$, is

$$E_{a,nom} = E_{g,0} + \frac{\alpha\beta T_{nom}^2}{(T_{nom}+\beta)^2}. \tag{3.11}$$

This leads to a T_{nom} referenced $E_{a,T}$

$$E_{a,T} = E_{a,nom} - \frac{\alpha\beta {T_{nom}}^2}{(T_{nom}+\beta)^2} + \frac{\alpha\beta T T_{nom}}{(T+\beta)(T_{nom}+\beta)}. \tag{3.12}$$

Including nonlinear $E_{g,T}$, the simulated I_C-V_{BE} at low temperature are is still far away from measurement as shown in Fig. 3.5. Clearly a new approach needs to be developed to improve T-scaling in current models.

[22] and [23] proposed to include a T-dependent N_F into $I_{S,T}$. Intuitively, the increase of N_F with temperature will gear down the decrease of I_S. Below we will show that using a T-dependent N_F in $I_{S,T}$ can significantly improve $I_C - V_{BE}$ fitting below 200K.

The including of $N_{F,T}$ leads to a $I_{S,T}$ function as

$$I_{S,T} = I_{S,nom}\left(\frac{T}{T_{nom}}\right)^{\frac{X_{IS}}{N_{F,T}}} \exp\left(\frac{-E_{a,T}\left(1-\frac{T}{T_{nom}}\right)}{N_{F,T}V_T}\right). \tag{3.13}$$

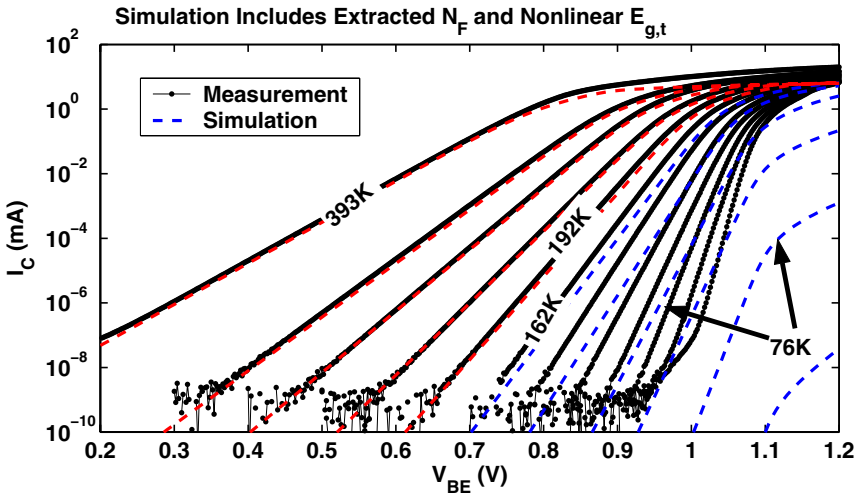

Figure 3.5: Simulated versus measured $I_C - V_{BE}$. Extracted N_F and Thurmond's $E_{g,T}$ included.

Table 3.1: Temperature scaling models examined in this work.

Name	Model 1	Model 2	Model 3
$N_{F,T}$	1.0	(3.2)	(3.2)
$E_{a,T}$	$E_{a,nom}$	$E_{g,0}$	(3.12)

Now we examine three models of different complexity shown in Table 3.1. Model 1 is the SGP model with N_F=1. Model 2 uses nonlinear $N_{F,T}$, but with E_a=$E_{g,0}$. This has been shown to be equivalent to using Lin and Salama's nonlinear bandgap model (also used in HICUM). Model 3 implements $N_{F,T}$ in (3.1) and (3.3).

Fig. 3.6 compares I_S modeling results for all three models. Model 1 gives several decades lower I_S below l00 K. Model 2 and 3 are both close to the extracted I_S and give comparable $I_{S,T}$ fitting. On closer examination, model 3 is better.

If $\beta = 0$ in (3.11), the nonlinear $E_{g,T}$ will be simplified as a linear equation. $E_{a,nom}$ in Model 3 will be equal to $E_{g,0}$. Model 3 with $\beta = 0$ can provide better fitting than Model 1, but worse fitting than Model 3 with $\beta = 686$.

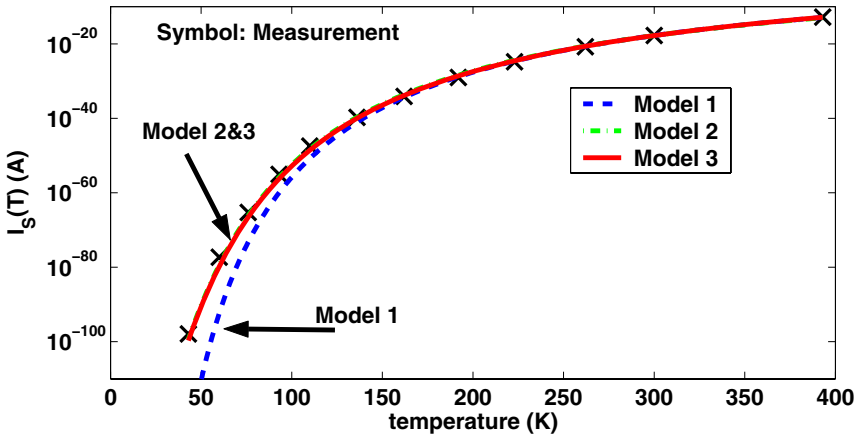

Figure 3.6: I_S extracted from measurement versus I_S from the three models listed in Table 3.1 over 43-400 K.

3.1.3 Summary

Fig. 3.7 compares the I_C-V_{BE} simulated with measurement. Above 110 K, even the simplest model, Model 1, can produce reasonably good $I_C - V_{BE}$ at moderate injection as shown in Fig. 3.7 (a). From 43-93 K, however, model 1 fails, as shown in Fig. 3.7 (b). Model 3 shows the best result at 43 K.

In model 3, if linear $E_{g,T}$ is used, i.e. $\beta = 0$, the resulting $E_{a,nom}$ is 0.028 eV lower than the $E_{a,nom}$ in model 3 from (3.11). Typical value $\alpha = 4.45e-4$ and $\beta = 686$ is used in (3.11). Although it looks like that model 2 is based on a linear $E_{g,T}$ model, with the choice of $E_{g,T} = E_{g0}$, it could be essentially applying the nonlinear $E_{g,T}$ model of Lin and Salama's [24]. Part of nonlinear coefficient of $E_{g,T}$ also appears as part of the X_{IS} term. In other words, both $E_{a,nom}$ and X_{IS} need to be adjusted for model 2 to work. This is also confirmed by simulation.

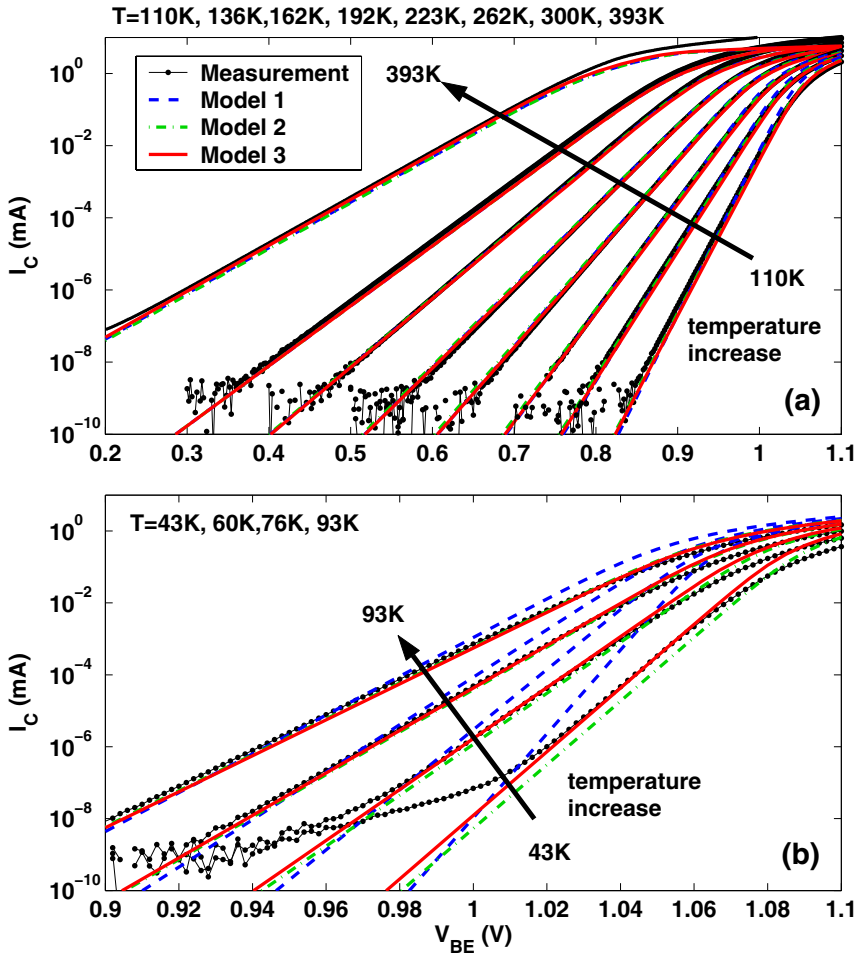

Figure 3.7: (a) Simulated versus measured I_C-V_{BE} at high temperatures. (b) Simulated versus measured I_C-V_{BE} at low temperatures.

3.2 N_F's Effect in Base Diffusion Charge

As including non-linear temperature dependent N_F into $I_C - V_{BE}$ is necessary, accordingly, to correctly model base diffusion charge, (2.25),(2.26), (2.27), (2.28), (2.31) and(2.33) should be adjusted to

$$I = \frac{2I_S \exp\left(\frac{V_{B_2E_1}}{N_{F,T}V_T}\right)}{1 + \frac{\tau_{BI}}{Q_{B0}}}, \tag{3.14}$$

$$I = \frac{2I_S \exp\left(\frac{V_{B_2E_1}}{N_{F,T}V_T}\right)}{1 + \sqrt{1 + \frac{4I_S}{I_K}\exp\left(\frac{V_{B_2E_1}}{N_{F,T}V_T}\right)}}, \tag{3.15}$$

$$I_{low} = I_S \exp\left(\frac{V_{B_2E_1}}{N_{F,T}V_T}\right), \tag{3.16}$$

$$I_{high} = \sqrt{I_S I_K} \exp\left(\frac{V_{B_2E_1}}{2N_{F,T}V_T}\right), \tag{3.17}$$

$$f_1 = \frac{4I_S}{I_K} \exp\left(\frac{V_{B_2E_1}}{N_{F,T}V_T}\right), \tag{3.18}$$

and

$$f_2 = \frac{4I_S}{I_K} \exp\left(\frac{V_{B_2C_2}}{N_{F,T}V_T}\right). \tag{3.19}$$

CHAPTER 4

BGR IMPLICATION

The temperature dependence of $I_C - V_{BE}$ is very important for bandgap reference (BGR) design. The main concept of BGR is to use the positive temperature coefficient of $\triangle V_{BE}$ generated by two transistors operating at different current densities to compensate the negative temperature coefficient of V_{BE}, to make a zero temperature coefficient reference voltage output [10]. As a strongly T-dependent ideality factor N_F has been included into $I_C - V_{BE}$ relation. ΔV_{BE}=$N_F V_T \ln(J_{C1}/J_{C2})$ is no longer linearly proportional to T.

In this Chapter, the three models in Table 3.1 in Chapter 3 are used to examine $V_{BE} - T$ and $\Delta V_{BE} - T$. Implication to BGR output is simulated with a Widlar BGR circuit.

4.1 $V_{BE} - T$

The V_{BE} versus T characteristics at three fixed I_C, I_C=0.1μA, 1μA, and 10μA, are shown in Fig. 4.1 (a). The data are interpolated from forward gummel measurement and simulation.

Above 200K, all three models can correctly model the nonlinear $V_{BE} - T$ dependence. Below 200K, although the deviation of simulated V_{BE} from measured V_{BE} is small, it is significant when normalized by thermal voltage, as shown in Fig. 4.1 (b).

4.2 $\Delta V_{BE} - T$

A Widlar BGR as Fig. 4.2 is built in ADS simulator using three models from Table 3.1 to evaluate the improvement of the new temperature dependence model in more realistic environment. All of the elements in BGR except the transistors are ideal components including the ideal current source I_0.

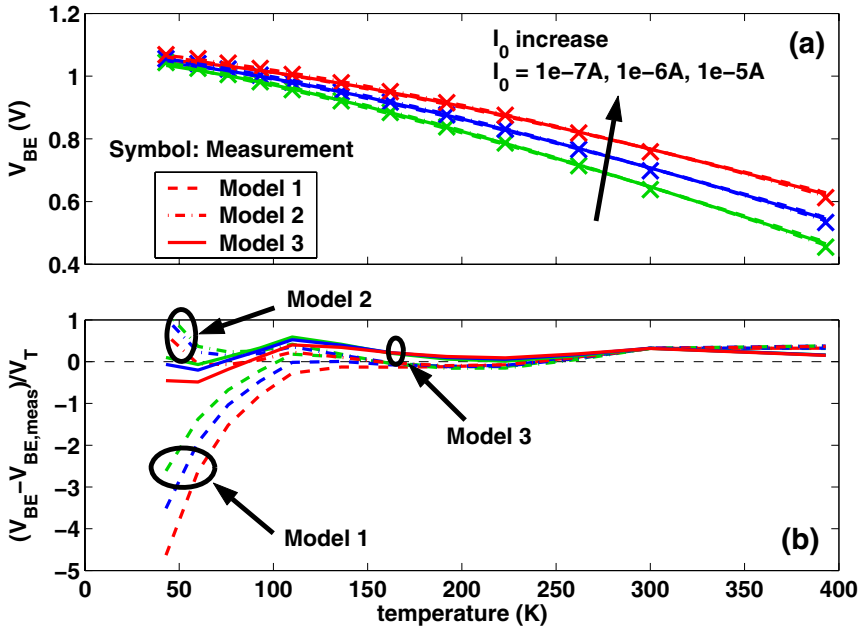

Figure 4.1: (a) Simulated versus measured V_{BE}-T dependence at I_0=0.1μA, 1μA, and 10μA. (b) Deviation of simulated V_{BE} from measured V_{BE} normalized by thermal voltage.

As for simulation, the V_{BE} difference, ΔV_{BE}=$V_{BE,1st}$-$V_{BE,2nd}$, is generated by two transistors having 8 times different current densities, whereas the measured $\triangle V_{BE}$ is actually interpolated from forward gummel data between two points which has 8 time current difference, as testing is not available.

Comparison between measurement and three models is plotted in Fig. 4.3 (a). Fig. 4.3 (b) shows $\Delta V_{BE}/V_T$. Model 1 gives a linear $\Delta V_{BE} - T$ dependence as expected. Model 2 and 3 can both reasonably reproduce the nonlinear temperature dependence of ΔV_{BE}. $\Delta V_{BE}/V_T$ is a constant above 200 K, and this constancy is the basis for producing a PTAT voltage in BGR design.

4.3 $V_{ref} - T$

Fig. 4.4 compares V_{REF}, the simulated output voltage of BGR, with measurement results. The measurement results in Fig. 4.4 (a), not from a real BGR circuit measured, is again the estimated V_{REF} using measured I_C-V_{BE} data, which provides a reference value for the comparison. V_{REF} using Model 1 is several V_T lower than measurement. Model 2 and 3 can dramatically improve the

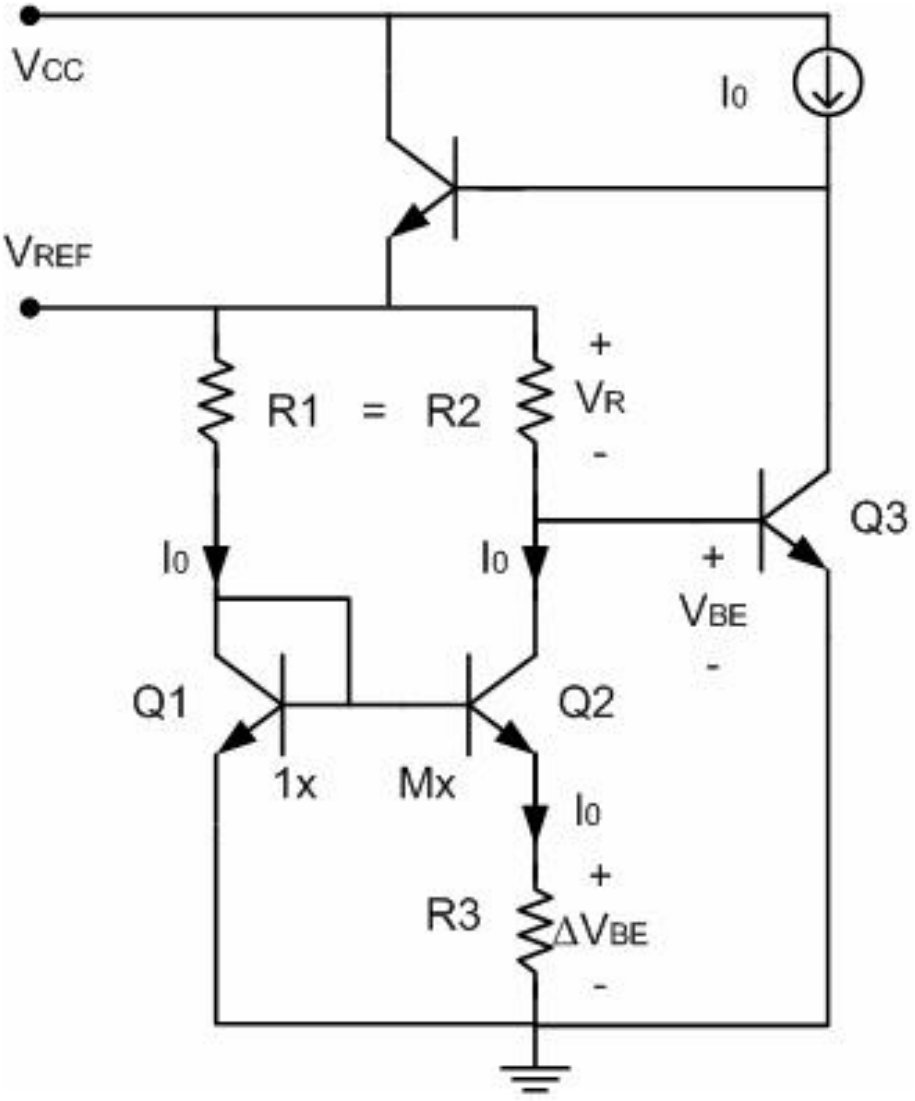

Figure 4.2: Wildar bandgap reference circuit.

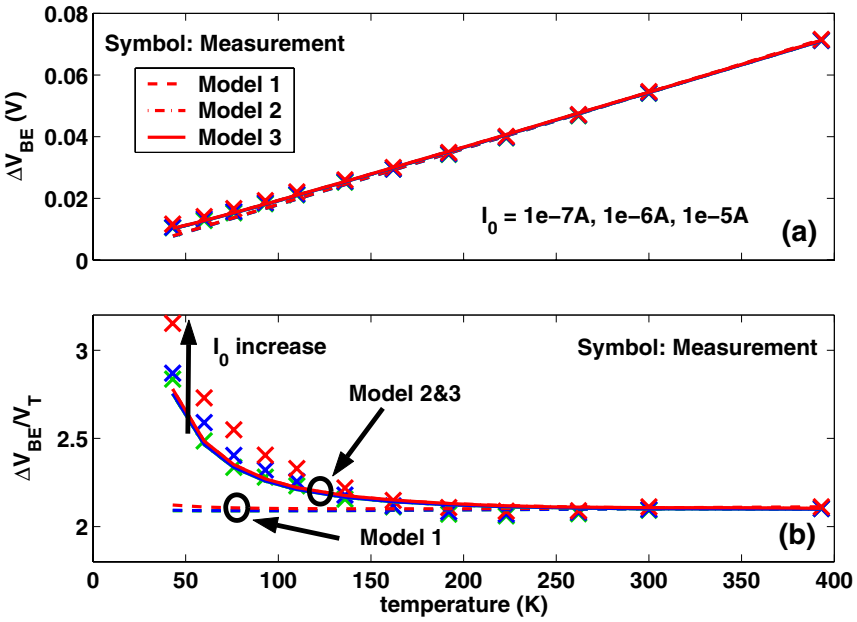

Figure 4.3: (a) Simulated versus measured $\Delta V_{BE} - T$ at I_0=0.1μA, 1μA, and 10μA. (b) Deviation of simulated ΔV_{BE} from measured ΔV_{BE} normalized by thermal voltage.

simulation results, and further benefit the simulation of large ICs. The increase of $\Delta V_{BE}/V_T$ and decrease of V_{ref} with cooling below 200 K may need to be considered and exploited for better BGR design at cryogenic temperatures.

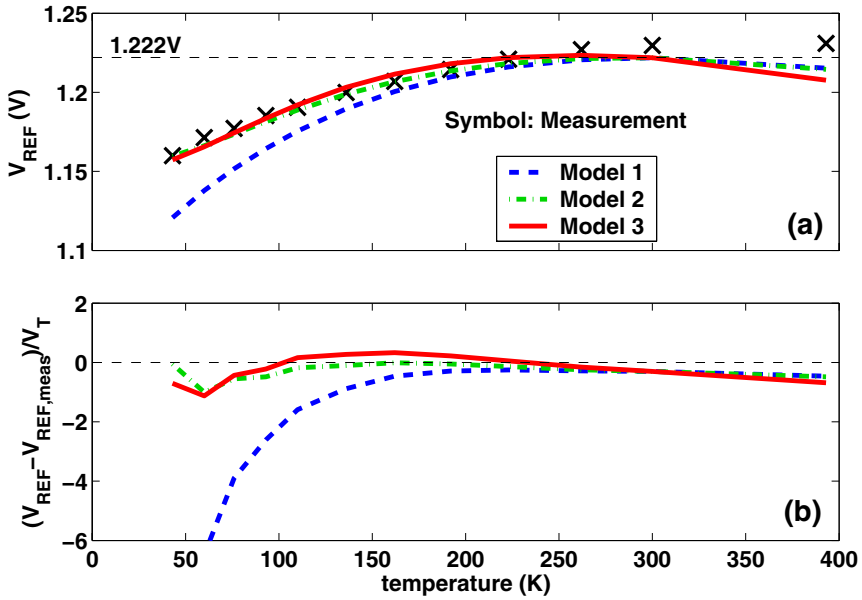

Figure 4.4: (a) Simulated V_{REF} versus measured V_{REF} for three models. (b) Deviation of simulated V_{REF} from measured V_{REF} with respect to thermal voltage.

CHAPTER 5

BASE CURRENT MODELING

This chapter addresses $I_B - V_{BE}$ characteristics. In Mextram, the $I_B - V_{BE}$ modeling is achieved in the use of current gain factor β_f and related to I_S. The current gain, however, as shown in Fig. 5.7 (a), varies strongly with bias at low temperature and becomes more I_C dependent. This will couple the inaccuracy of I_C modeling into I_B and make the extraction more complex.

Here, the same strategy used in I_C modeling is used for "ideal" I_B. Saturation current and ideality factor of I_B itself will be used in the model, which will facilitate the modeling by avoiding unnecessary entanglement.

At low temperature, the base current has a obvious increase in low bias range, which makes the curve deviate from linearity. The excess current is contributed by forward-bias tunneling, i.e., trap-assisted tunneling (TAT). We find that ideality factor extracted from $I_B - V_{BE}$ moderate region is exaggerated to some extent at low temperature because of tunneling current, while it only happens at 43 K in $I_C - V_{BE}$. Using a method of iteration, we can separate the main base current and tunneling current and quantify the effect of tunneling on the total current gain falloff at low temperature. A new temperature scaling of tunneling saturation current equation is proposed by including ideality factor $N_{E,TAT}$.

5.1 Trap-Assisted Tunneling Effect

It has already been found that tunneling generation is an important source of leakage in advanced silicon device [25] [26] [27] [28]. The trend of down scaling and high doping in device technology leads to a strong electric field around the p-n junction, making the effect of tunneling significant [29].

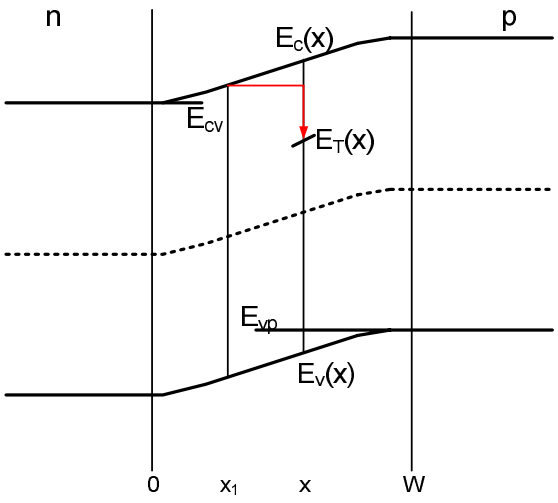

Figure 5.1: Illustration of trap-assisted tunneling in forward biased EB junction.

Generally, when the E-B junction is reversed biased, band-to-band tunneling (BBT) dominates due to the overlap between valance band in the base region and conduction band in the emitter region [30]. When the E-B junction is forward biased, the base current increase is mainly due to TAT, which is the case of this work. Under the later circumstances, a defect with an energy state deep in the band gap, called a "trap", assists the tunneling process shown in Fig. 5.1. An electron located at x_1 can tunnel to a trap at x later recombines with a hole tunneling to x. The higher doping level is, the easier it is to observe this phenomenon [31]. For collector current the tunneling process is more complicated [3].

Fig. 5.2 (a) and (b) show the gummel measurement data. For our device, the TAT current in I_C can be only observed at 43K while can be observed in I_B below 110K. This is the reason for current gain falloff at low temperature [32] [31], which will also be proved later. The tunneling current can be mainly observed at high doped E-B junction and hardly seen at low doped C-B junction. This is consistent with reverse gummel I_E and I_B shown in Fig. 5.2 (c) and (d).

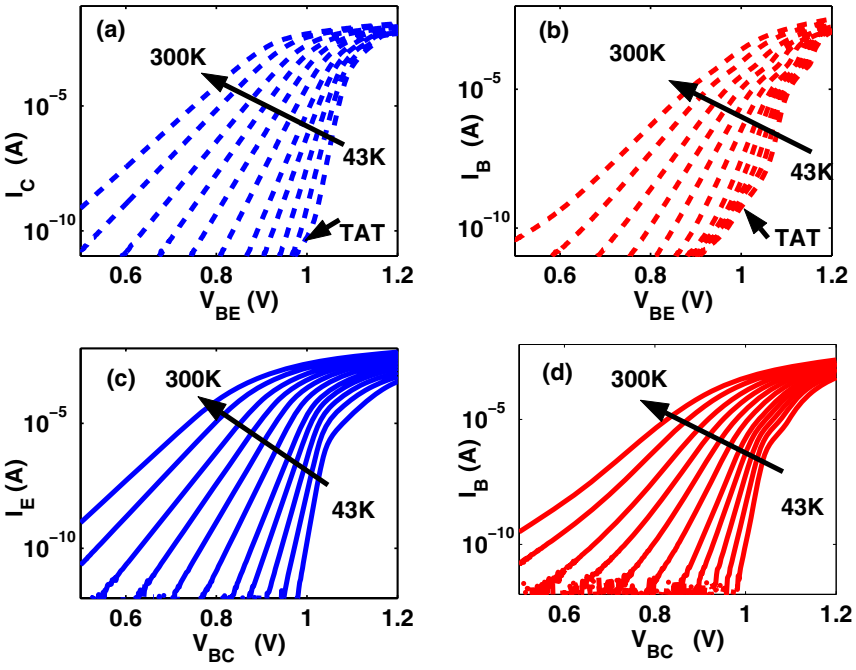

Figure 5.2: Forward and reverse gummel measurement data: (a) forward gummel I_C-V_{BE}, (b) forward gummel I_B-V_{BE}, (c) reverse gummel I_E-V_{BC} and (d) reverse gummel I_B-V_{BC}.

5.2 Separation of Main and Tunneling Base Current

As the base tunneling current is not negligible below 110K, we definitely need to accurately estimate the magnitude of tunneling current and quantify its effect on the main base current. In other words, the tunneling current has to be taken off from total base current, avoiding overvaluing main current.

Below, we use a iteration method to separate the main and tunneling current:

1) Select a linear region on $I_B - V_{BE}$ and perform linear fitting. Extract slope and intercept of this part.

2) Subtract the linear fitting from total base current and get a nearly linear line at low V_BE region. Linear fitting is again performed for this low V_{BE}.

3) Subtract fitting result obtained by Step 2 from total I_B.

4) Perform linear fitting on the result obtained by Step 3. Extract slope and intercept again.

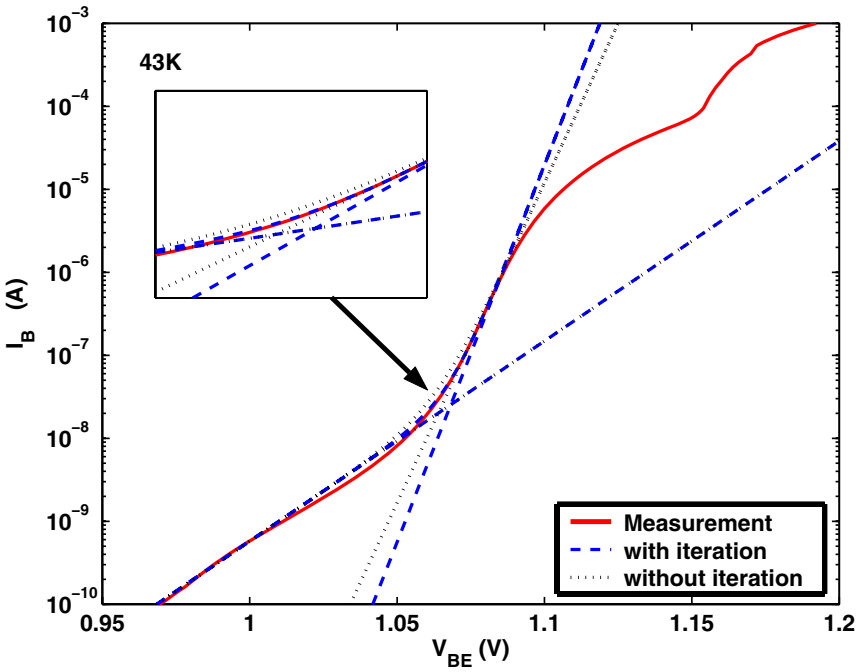

Figure 5.3: Difference between linear fitting with and without iteration at 43 K.

5) Repeat the Step 2, 3 and 4 until the difference of slope extracted by two successive times is smaller than a set limit.

Fig. 5.3 shows the difference between linear fittings of base current with and without iteration at 43 K. Without iteration means that main current is directly fitted only by Step 1 from the a certain region without excluding the tunneling current. The slope including tunneling current is smaller than that excluding tunneling current, increasing ideality factor from 1.290 to 1.522, a significant number. The saturation current is correspondingly downgraded. A zoom-in plot shows the with iteration the summation of two linear fitting can better fit the measurement. The same method is applied on $I_C - V_{BE}$ only at 43 K.

5.3 Ideality Factor, Saturation Current and Current Gain

Using the method proposed above, we are able to accurately extract the ideality factors and saturation currents of main base and collector currents. Fig. 5.4 shows the extracted saturation

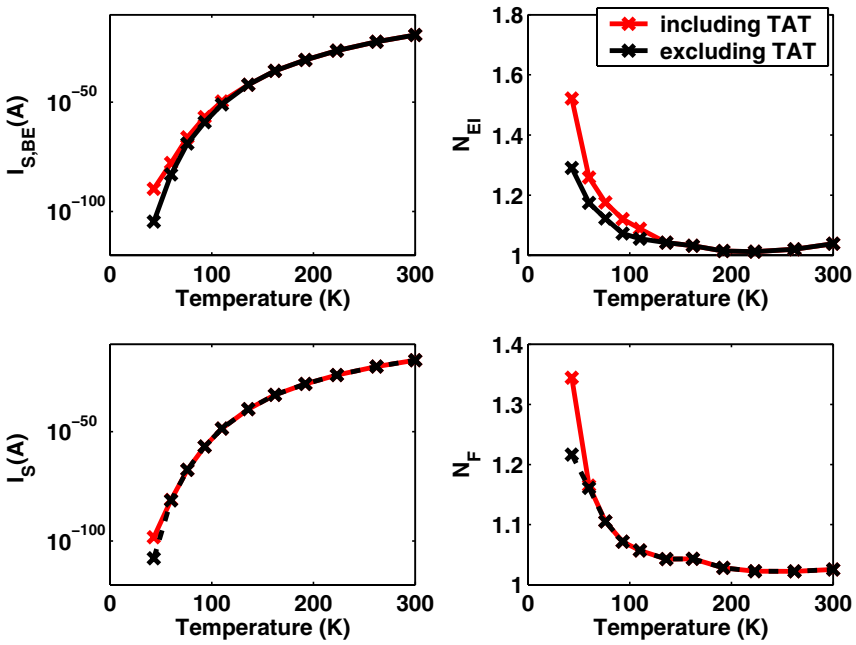

Figure 5.4: Comparison of ideality factor and saturation current between including and excluding TAT current: (a) $I_{S,BE}$-T, (b)N_{EI}-T, (c) I_S-T, (d)N_F-T.

currents and ideality factors. "Excluding TAT" means the results are obtained from the ideal base current, i.e., subtracting tunneling current from total base current. It is clear that excluding the TAT current will result in smaller ideality factor and larger saturation current especially for low temperature.

Comparing the base saturation current with collector saturation current, we find that the I_{BEI} has weaker temperature dependence than I_S as shown in Fig. 5.5. The slopes of $I_C - V_{BE}$ and $I_B - V_{BE}$ extracted from Hydrodynamic simulation, measurement are overlaid in Fig. 5.6. The slope of simulated $I_C - V_{BE}$ is smaller than ideal $1/V_T$ at temperature below 100 K, while that of $I_B - V_{BE}$ is almost same as ideal $1/V_T$. The difference is mainly caused by early effect and Ge-ramp effect. The slopes of both $I_C - V_{BE}$ and $I_B - V_{BE}$ extracted from measurement excluding tunneling current are larger than those of including tunneling current, but still smaller than those of simulation. This verifies that the ideality factor larger than 1 at low temperature [9] is substantial and at least not due to tunneling current. The freezeout model has not been applied in simulation, so freezeout effect may be responsible for that. However the freezeout should not affect highly doped

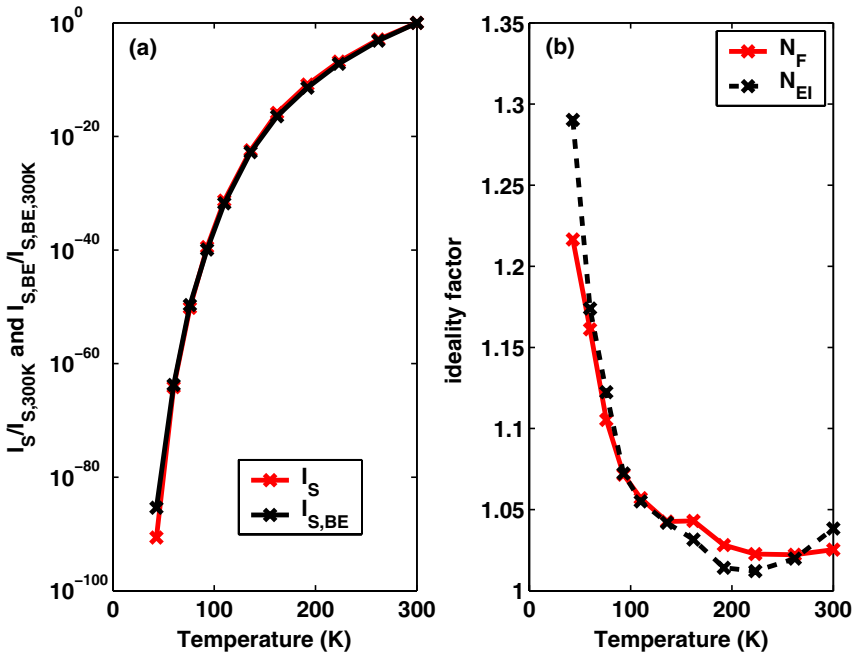

Figure 5.5: Comparison of ideality factor and saturation current between collector and base: (a) saturation current, (b)ideality factor.

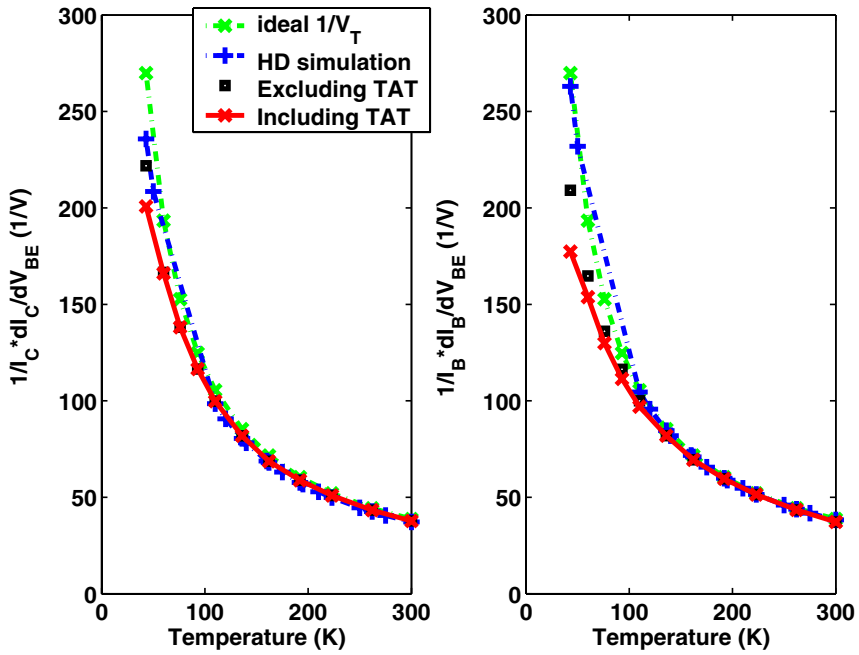

Figure 5.6: The slopes of (a) $I_C - V_{BE}$ and (b) extracted from simulation and measurement from 43 to 300 K.

emitter much and base ideality factor is also larger than 1, therefore the physics underneath needs further exploration.

Next we exam the effect of tunneling on current gain. Fig. 5.7 (a) is obtained by directly dividing measured I_C by I_B. Fig. 5.7 (b) only by dividing main I_C by main I_B, which means the TAT effect has been excluded. The current gain now does not fall off but increases with cooling.

5.4 Tunneling Base Current Modeling

We have separated tunneling current from main current. We will focus at 43, 60, 76, 93 and 110 K to develop the tunneling current model.

The trap-assisted tunneling effect has been described by an expression that for weak electric fields reduces to the conventional Shockley-Read-Hall expression for recombination via traps and the model has one extra physical parameter, the effective mass m^* [29]. This method, however, is more preferably used in device simulations.

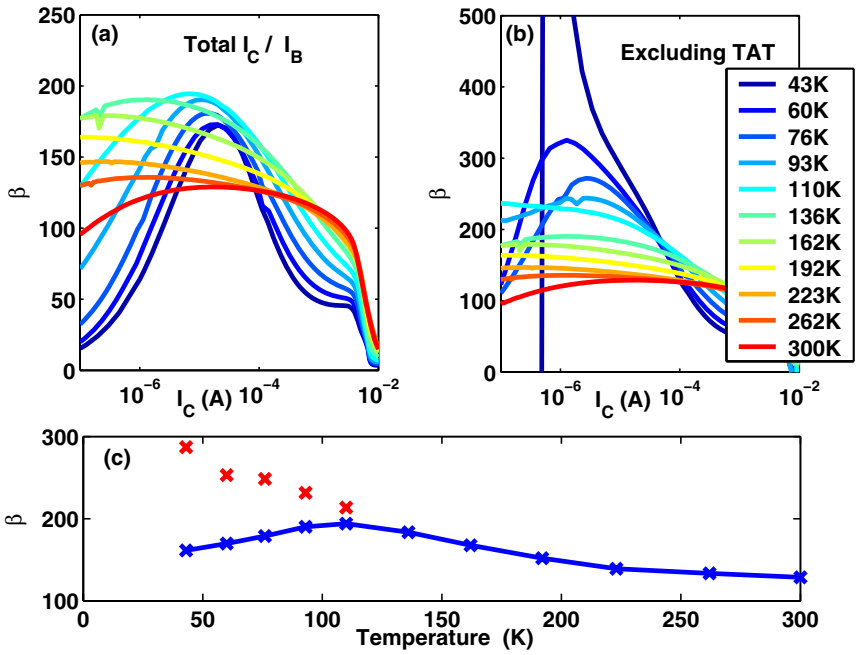

Figure 5.7: Comparison between current gain obtained by (a) total I_C/I_B and (b)excluding tunneling current and current gain obtained at $I_C = 10^{-5}$ A (c) by (a) and (b).

Fig. 5.8 (a) shows the tunneling current at these five temperatures. In the semilog scale, the current is not strictly linear line. However, we have found that two linear fittings in semilog scale is sufficient to model the total base current before high injection. So an exponential $I - V$ relation is sufficient and we need to carefully select the fitting range to get the ideality factor $N_{E,TAT}$ and saturation current $I_{S,BE,TAT}$. Fig. 5.8 (b) shows $N_{E,TAT}$ at five temperatures and it is proportional to $1/T$.

In most of the widely used compact models, such as Spice Gummel Poon, VBIC and Mextram, the non-ideal base current, i.e., base current at low bias, is modeled by Shockley-Read-Hall recombination [33] in an expression like

$$I_{BEN} = I_{S,BEN} \exp\left(\frac{V_{BE}}{N_{EN} V_T}\right), \tag{5.1}$$

in which N_{EN} is constant equal to 2.

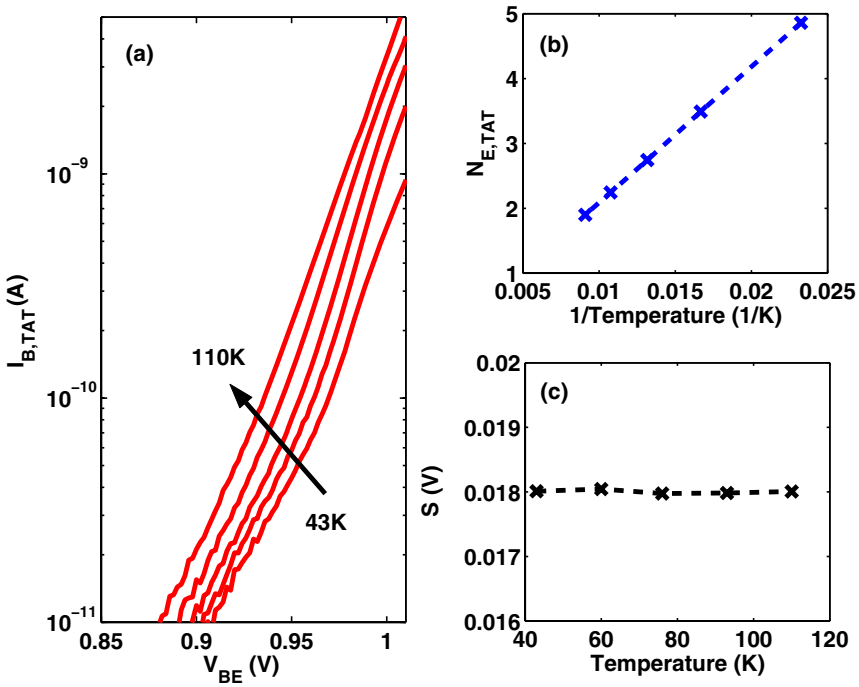

Figure 5.8: (a) Base tunneling current at 43, 60 76, 93 and 110 K; (b) The extracted ideality factor is proportional to $1/T$; (C) $S = N_{E,TAT} \times V_T$.

In our case, the $N_{E,TAT}$ increases from 1.9 at 110 K to 4.8 at 43 K, indicating that TAT current is dominant in low bias region at very low temperature. Besides, we found that $S = N_{E,TAT} \times V_T$ is independent of temperature. So here

$$I_{BE,TAT} = I_{S,BE,TAT} \exp\left(\frac{V_{BE}}{S}\right), \tag{5.2}$$

which is similar to [25], is added in addition to (5.1).

Temperature dependence of tunneling saturation current $I_{S,BE,TAT}$ in [25] comes from built-in potential ϕ_{bi}. As E-B junction doping is very high in our device, then $q\phi_{bi} = Eg$.

So firstly, we model the temperature dependence of $I_{BE,TAT,T}$ as

$$I_{S,BE,TAT,T} = I_{S,BE,TAT,0} \exp\left(-k_1 E_{g,T}\right). \tag{5.3}$$

Both linear

$$E_{g,T} = E_{g,0} - \alpha T \tag{5.4}$$

and nonlinear

$$E_{g,T} = E_{g,0} - \frac{\alpha T^2}{\beta + T} \tag{5.5}$$

are used and model results compared with extraction from measurement are shown in Fig. 5.9. The more accurate non-linear bandgap T scaling gives worse results than linear bandgap T scaling. so we propose to include $N_{E,TAT}$ which has a negative temperature coefficient into the modeling and get

$$I_{S,BE,TAT,T} = I_{S,BE,TAT,0} \exp\left(\frac{-k_1 E_{g,T}}{N_{E,TAT,T}}\right). \tag{5.6}$$

Making it related to the reference temperature,

$$I_{S,BE,TAT,T} = I_{S,BE,TAT} \exp\left(\frac{k_1 E_{g,ref}}{N_{E,TAT}} - \frac{k_1 E_{g,T}}{N_{E,TAT,T}}\right). \tag{5.7}$$

$I_{S,BE,TAT}$, E_g and $N_{E,TAT}$ are therefore the tunneling saturation current, bandgap and ideality factor at referenced temperature, which is normally 300 K. The modeling result is also shown in Fig. 5.9 and gives a equally good fitting using only linear $E_{g,T}$.

Replacing $N_{E,TAT}$ with S/V_T can reduce the number of parameters. So

$$I_{S,BE,TAT,T} = I_{S,BE,TAT} \exp\left(\frac{k_1}{S}\left(\frac{E_{g,ref}}{V_{T,ref}} - \frac{E_{g,T}}{V_T}\right)\right), \tag{5.8}$$

and k_1/S can be replaced by only one parameter, and $I_{S,BE,TAT}$ is tunneling saturation current at reference temperature. Hence,

$$I_{S,BE,TAT,T} = I_{S,BE,TAT} \exp\left(k_1\left(\frac{E_{g,ref}}{V_{T,ref}} - \frac{E_{g,T}}{V_T}\right)\right). \tag{5.9}$$

The modeling results for 43 to 110 K are shown in Fig. 5.10 (b). Good fitting results of tunneling current are obtained.

5.5 Moderate Bias Region

Similar to I_C, the equation (2.38) and (2.39) of I_{B_1}, the "ideal" base current, are now adjusted to

$$I_{B_1} = \left(1 - XI_{B_1}\right) I_{BEI,T}\left(\exp\left(\frac{V_{B_2E_1}}{N_{EI,T}V_T}\right) - 1\right) \tag{5.10}$$

and

$$I_{B_1}^S = XI_{B_1} I_{BEI,T}\left(\exp\left(\frac{V_{B_1E_1}}{N_{EI,T}V_T}\right) - 1\right). \tag{5.11}$$

$I_{BEI,T}$ and $N_{EI,T}$ are temperature scalable forward base saturation current and forward base ideality factor. Good fitting results combined with tunneling current results against measurement are shown in Fig. 5.10 (a) for 43 to 100 K. The same has been implemented in I_{EX} to model reverse base current.

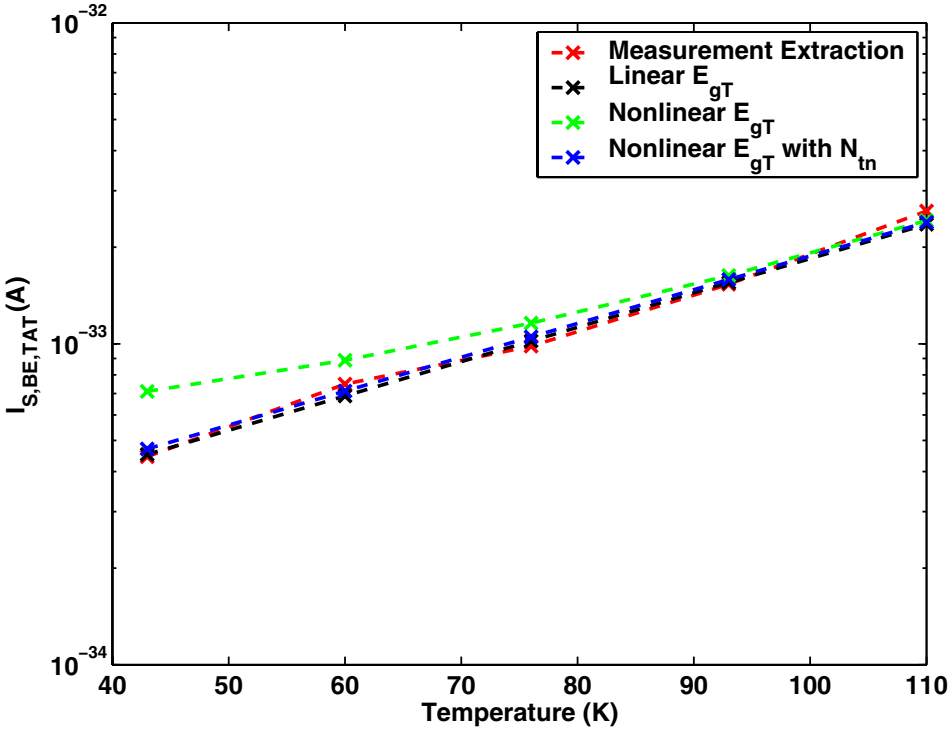

Figure 5.9: The temperature scaling of tunneling saturation current at 43, 60, 76, 93 and 110 K.

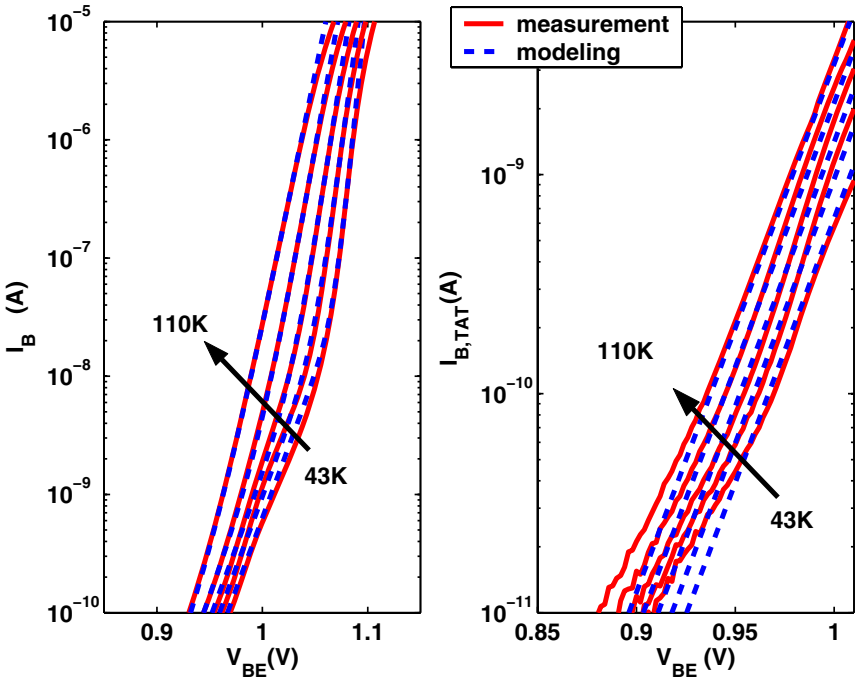

Figure 5.10: Comparison between measurement an modeling results for 43 to 110 K: (a) combined with ideal base fitting, (b) TAT current modeling

.

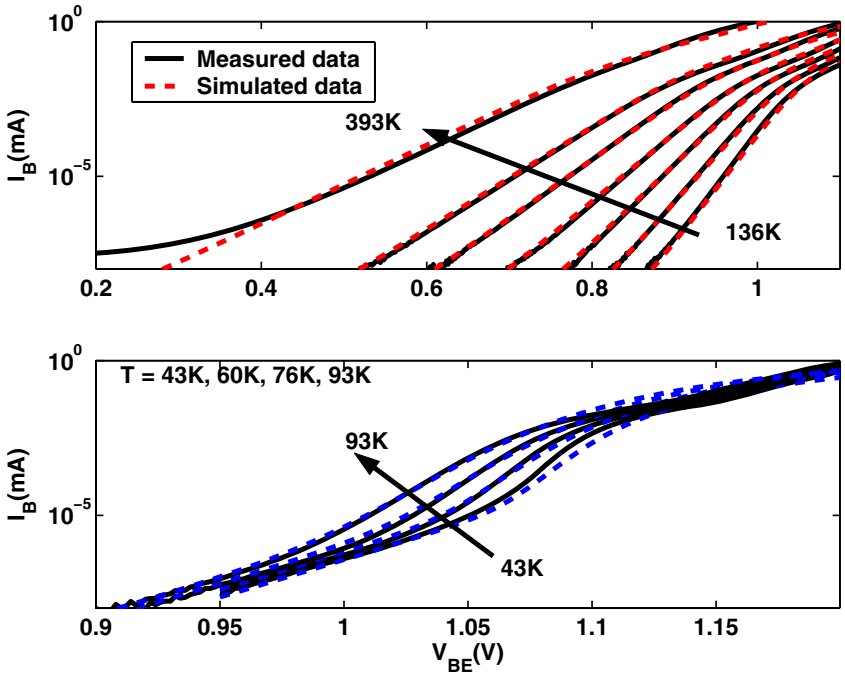

Figure 5.11: Measured and modeled I_B-V_{BE} from 43-93 K.

5.6 Summary

Fig. 5.11 show the $I_B - V_{BE}$ results from 43-393 K. New I_B model for moderate and low bias region work together to give a good simulation result over the whole temperature range.

CHAPTER 6

SMALL SIGNAL MODELING

Small signal modeling is an important tool used for parameter extraction and linear RF circuit design. As SiGe HBTs are widely used in RF circuit, here the small signal equivalent circuit will be used to discuss the device RF performance. Most of the work has been published in [8].

6.1 Equivalent Circuit

Fig. 6.1 and Fig. 6.2 shows the small-signal equivalent circuit used in this work. This is a typical equivalent circuit for SiGe HBTs, with a topology similar to the large-signal equivalent circuit in compact models such as VBIC and Mextram. An exception is the addition of the C_{cso} capacitance, which in addition to C_{cs} and R_s is necessary to fit the imaginary part of Y_{22}. This capacitance was proposed in [34], but was attributed to the overlapping of the emitter and collector interconnection metals. We believe, however, that this C_{cso} is physically the peripheral deep trench coupling capacitance between the N^+ buried layer and p-substrate. Note that such a capacitance has not been used in other investigations (e.g., [35]).

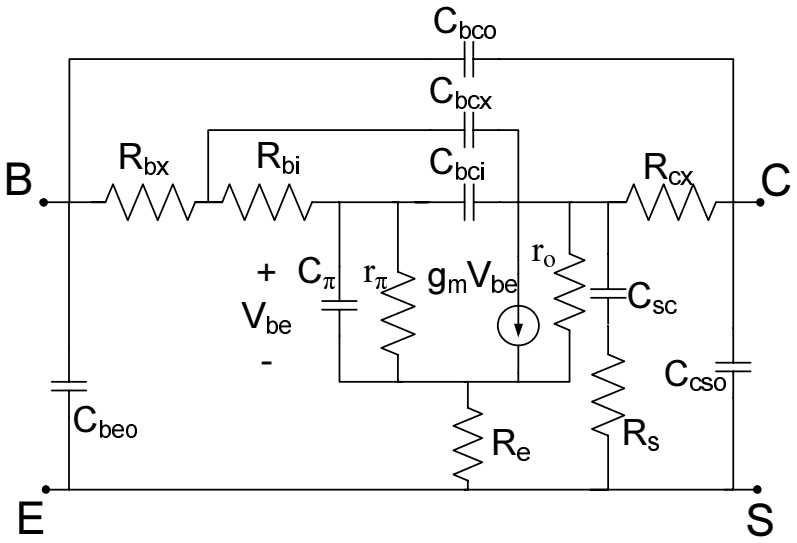

Figure 6.1: Small-signal equivalent circuit used for SiGe HBTs.

6.2 Parameter Extraction

Fig. 6.3 shows the measured f_T-I_C as a function of V_{CB} at 300, 223, 162 and 93 K. With cooling, peak f_T increases, and the f_T roll-off current increases as well. To make the parameter extracted at each temperature comparable, similar I_C points are chosen for each T as shown in Fig. 6.4. The higher V_{BE} range is chosen to cover the rise and fall portions of the f_T-I_C curves. At each temperature, hot S-parameter measurements were made on-wafer from 1 to 35 GHz by sweeping V_{BE} for $V_{CB} = -0.5$, 0, 1, and 2 V.

6.2.1 Procedure

There have been several direct extraction methods reported for SiGe HBTs [34] [35]. However, these methods do not yield good results when applied to the present data. Here a combination of direct extraction and a two-step optimization procedure is chosen, as detailed below.

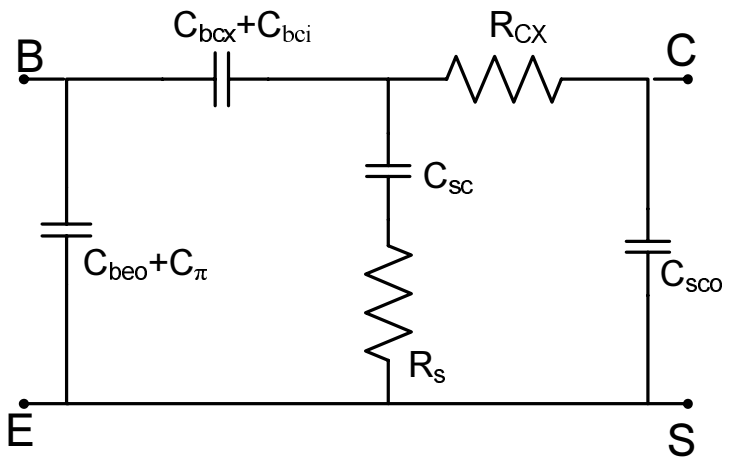

Figure 6.2: Small-signal equivalent circuit used for cold state.

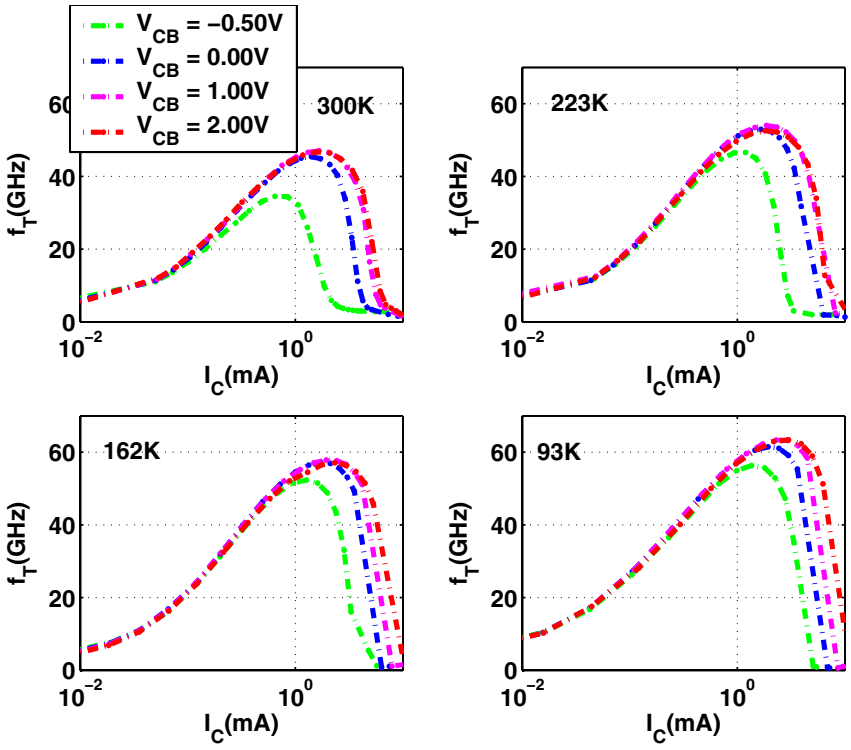

Figure 6.3: Measured f_T-I_C as a function of V_{CB} at various temperatures.

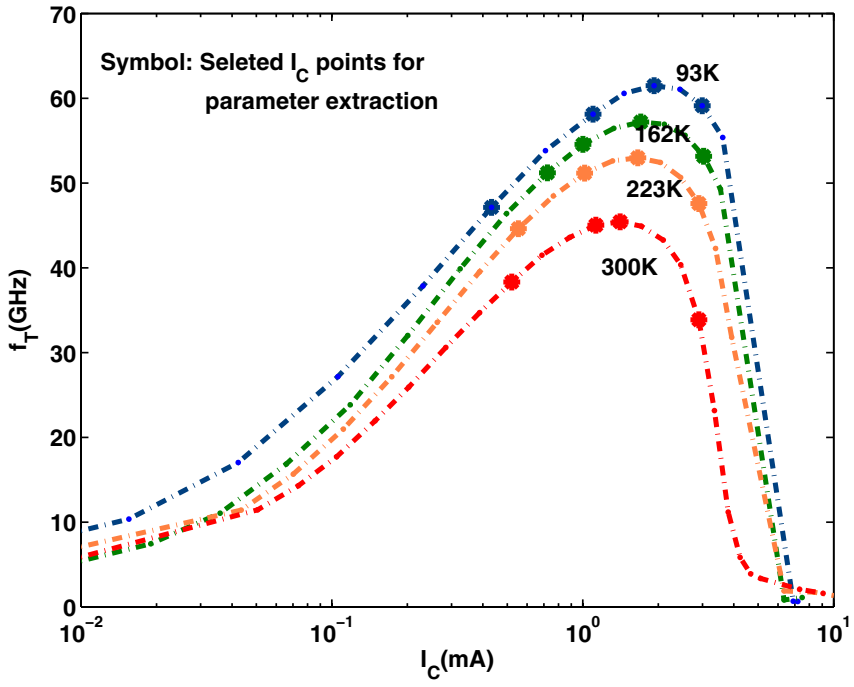

Figure 6.4: Selected I_C points for each temperature extraction .

A common first step in [34] [35] is extracting C_{beo} and C_{bco} from cold Y-parameter data. The total C_{be} is obtained from imaginary part of $Y_{11}+Y_{12}$ for each V_{BE}, and then fitted into C_{be}= C_{beo} + $C_{je}(1+V_{be}/V_{de})^{-M_{je}}$. Our experience shows that this approach is very unreliable, as many solutions exist for C_{beo}, C_{je}, V_{de} and M_{je}. Furthermore, it is found that in order to fit the imaginary part of Y_{11} above 20 GHz, C_{beo} must be allowed to increase with I_c. The exact physical origin of this increase of C_{beo} with I_c is not yet well understood. It could, for instance, be a manifestation of sidewall injection which is not explicitly accounted for in this equivalent circuit. The most reliable way to extract C_{beo}, is to use optimization of the imaginary part of Y_{11} for hot data (Y-parameters measured at higher V_{BE} when device is turned-on), as it contributes to $\Im(Y_{11})$. During optimization, the value of C_{bco} constantly approaches zero, at which we fixed C_{bco} accordingly.

One main disadvantage of optimization is the multiple and sometimes unphysical solutions that result. When optimization is directly used on hot Y-parameters without constraints, the resulting C_{bci} tends to be unrealistically small, and the V_{cb} and I_c dependence of C_{bci}, C_{bcx}, C_{cs} and R_s are

not physical. This problem is overcome by fitting the cold Y-parameters first to determine C_{cso}, C_{cs}, and R_s first. These parameters are then fixed for the required V_{CS}. Two sets of cold measurements were taken, one V_{CB} sweep at V_{BE}=0 V, and one V_{BE} sweep at V_{CB}=0 V. In the cold state, it is not possible to distinguish C_{bci} from C_{bcx}, or to distinguish C_{beo} from C_{π}, and thus a simplified circuit, as shown in Fig. 6.2, is used. C_{cso} is found to be independent of V_{BE} or V_{SC}. C_{cso} is 3 fF at 300 K, and weakly temperature dependent. We believe C_{cso} is the peripheral coupling capacitance between buried layer and p-substrate through the deep trench oxide. C_{cs} decreases slightly with V_{CS}, as expected.

Next, R_e is extracted from a standard R_e flyback measurement. R_e is very difficult to uniquely determine from optimization. The R_e from optimization is much larger than the R_e from flyback, and can be bias dependent, which is unphysical. Another parameter that is equally difficult to uniquely determine from optimization is R_{bx}. Here it is determined from the high I_B limit of an overdriven measurement. R_e and R_{bx} are fixed over bias, and found to be temperature independent as well. R_e=6 Ω and R_{bx}=25 Ω for the device are used. All other parameters are then determined by fitting the hot Y-parameter over frequency data. This process is then repeated for each bias step.

6.2.2 Result

Fig. 6.5, 6.6, 6.7, 6.8 show the Y-parameter modeling results at 300, 233, 162 and 93 K. V_{CB}=0V was used here. Equally good fitting is achieved at other V_{BE}'s, except at high injection biases well after the f_T roll-off, where the equivalent circuit begins to fail. The real part of Y_{11} above 30 GHz at higher I_C is not yet well-fitted with the present circuit. The attempt to include distributive effects (by adding a parallel capacitance to R_{bi}) and input non-quasi-static (NQS) effects (by adding a delay resistance to the diffusion component of C_{π}) did not further improve Y_{11} fitting. The measured imaginary part of Y_{11} shows a drop above 25 GHz, which cannot possibly be fitted with the equivalent circuit. As this occurs only at 93 K, The conclusion is likely due to measurement error, but this is still being explored. In general, both measurements and modeling become more difficult at 93 K.

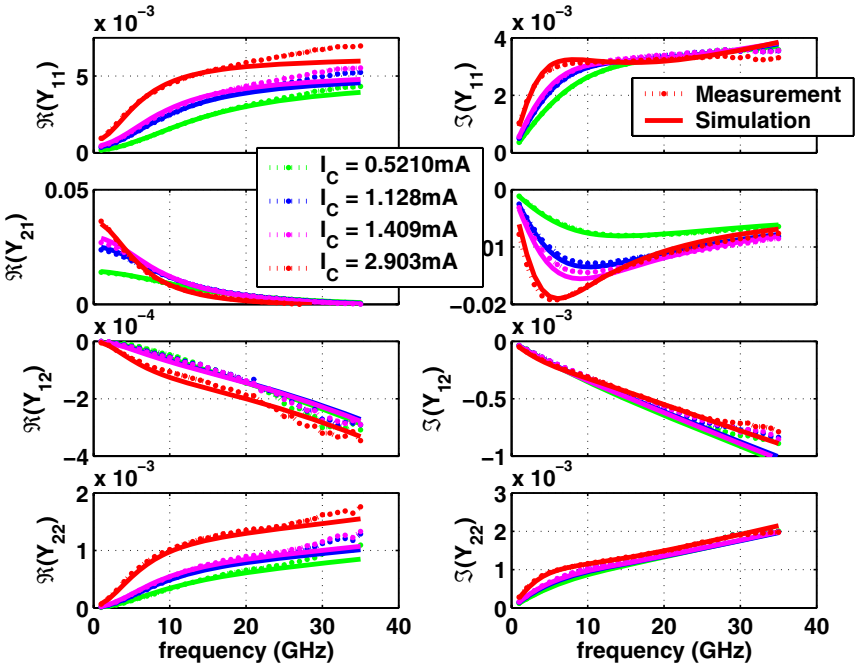

Figure 6.5: Measured and simulated Y-parameters at 300 K.

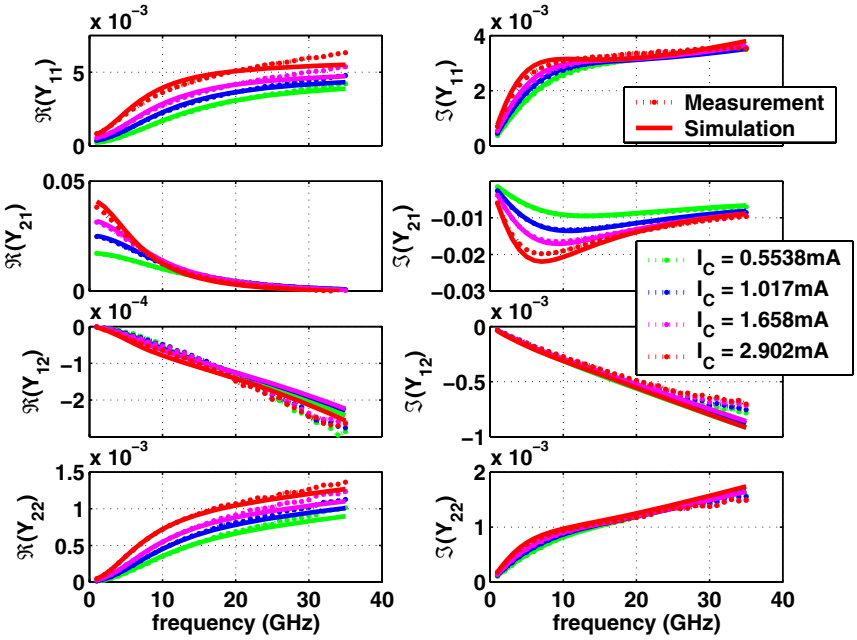

Figure 6.6: Measured and simulated Y-parameters at 223 K.

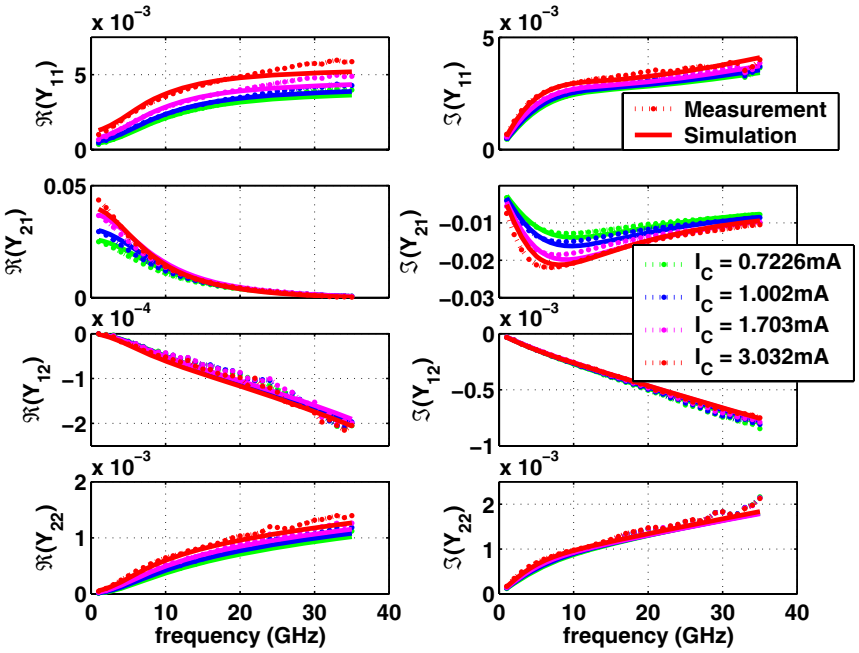

Figure 6.7: Measured and simulated Y-parameters at 162 K.

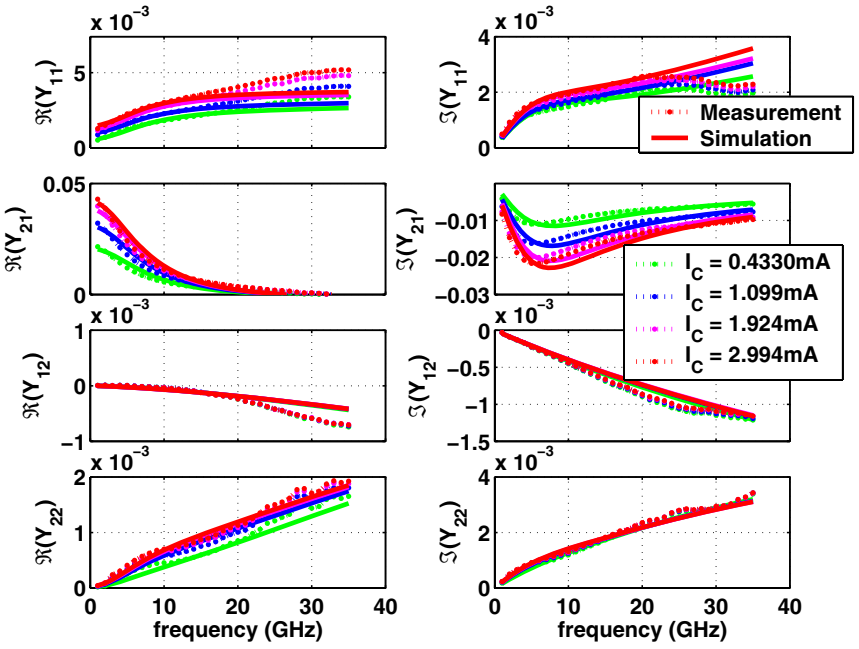

Figure 6.8: Measured and simulated Y-parameters at 93 K.

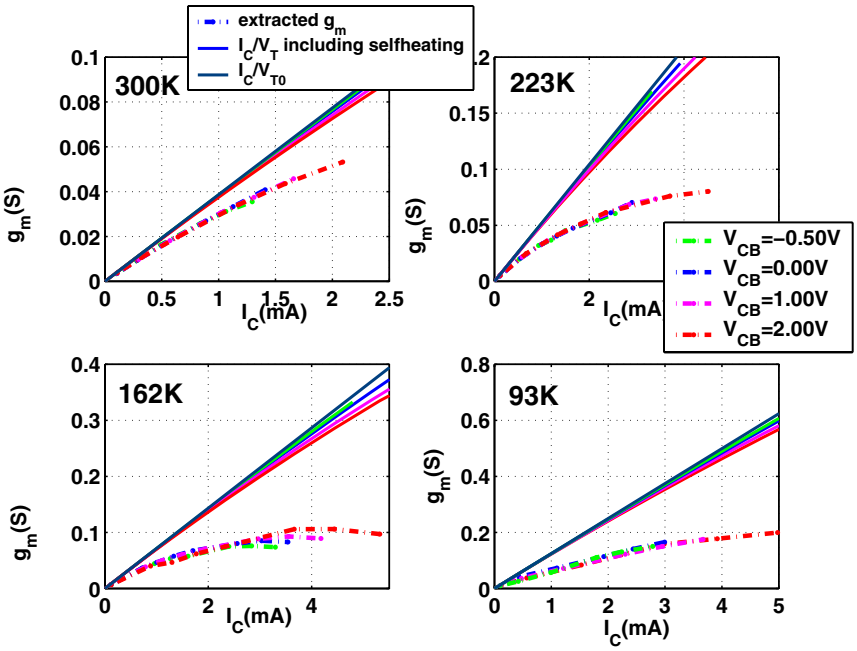

Figure 6.9: Extracted g_m-I_C results compared with ideal I_C/V_T with and without self-heating at 300, 223, 162 and 93 K.

Fig. 6.9 shows extracted g_m-I_C as a function of V_{CB}. The I_C/V_T both with and without self-heating are also shown as base-line references. R_{th} is extracted at each temperature using the method in [36]. A significant deviation of g_m from ideal I_C/V_T is observed, and the deviation increases with I_C. Note that the degradation of g_m compared to I_C/V_T is significant even before peak f_T. Interestingly, for different V_{CB}, as long as I_C is the same, g_m is approximately same. This means despite the complex impact of V_{CB} on I_C at high injection, the device intrinsic transconductance remains the same at a given I_C. This has direct implications on high frequency analog circuit biasing, as V_{CB} does not affect g_m as long as the biasing current can be fixed (e.g. with a current source).

Fig. 6.10 shows the extraction results of C_π-I_C. Again, little V_{CB} dependence is observed, even for V_{CB}=-0.5 V, which shows an early turn-on of Kirk effect. This early turn-on of Kirk effect at V_{CB}=-0.5 V is manifested through a rapid rise of the intrinsic CB capacitance C_{bci}, as shown below. Although g_m-I_C shows deviations from linearity, C_π-I_C is to a large extent linear, even past peak f_T. This leads to a rapid rise of the diffusion transit time with increasing I_C.

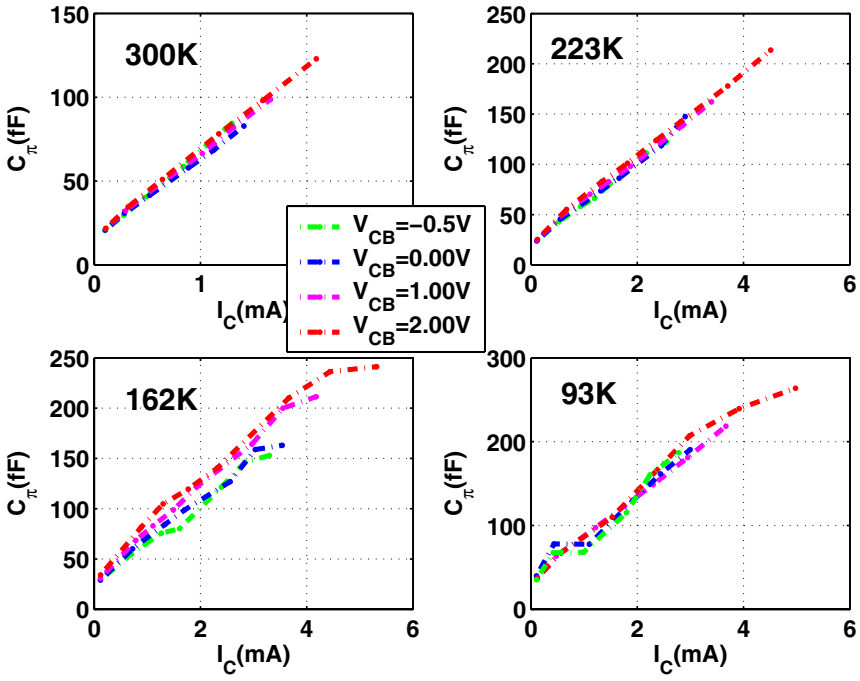

Figure 6.10: Extracted C_π-I_C at 300, 223, 162 and 93 K.

Fig. 6.11 shows the extracted C_{bci}-I_C and C_{bcx}-I_C results. Both C_{bci} and C_{bcx} decrease with increasing V_{CB}. C_{bci} increases with I_C, as expected, which is stronger at lower V_{CB}, while C_{bcx} is independent of I_C. This is physically meaningful since Kirk effect primarily occurs at the intrinsic selectively implanted collector (SIC) region. Kirk effect is the worst at V_{CB}=-0.50 V, causing the rapid increase of C_{bci} with I_C at V_{CB}=-0.50 V. Observe that the increase of C_{bci} with I_C corresponds to f_T rolling off. At low injection, both C_{bci} and C_{bcx} show a weak temperature dependence.

The total C_{bc} ($C_{bci} + C_{bcx}$) vs V_{BE} are shown in Fig. 6.12. The extraction results from cold data fitting (only V_{CB} =0 V is taken) are combined with results from hot data fitting. Observe that the cold and hot extraction results are very consistent.

The temperature dependence of R_{bi} and R_s are shown in Fig. 6.13. The bias dependence of R_s is very weak, as expected. R_{bi} shows the usual bias dependence, and here we use the R_{bi} extracted at I_C=1 mA. With cooling, R_s decreases from 3313 Ω at 300 K to 335.3 Ω at 93 K, while R_{bi} increases from 239.6 Ω at 300 K to 563.3 Ω at 93 K. This difference is caused by different doping levels in the p-substrate and p-base. The higher base doping level leads to much stronger impurity

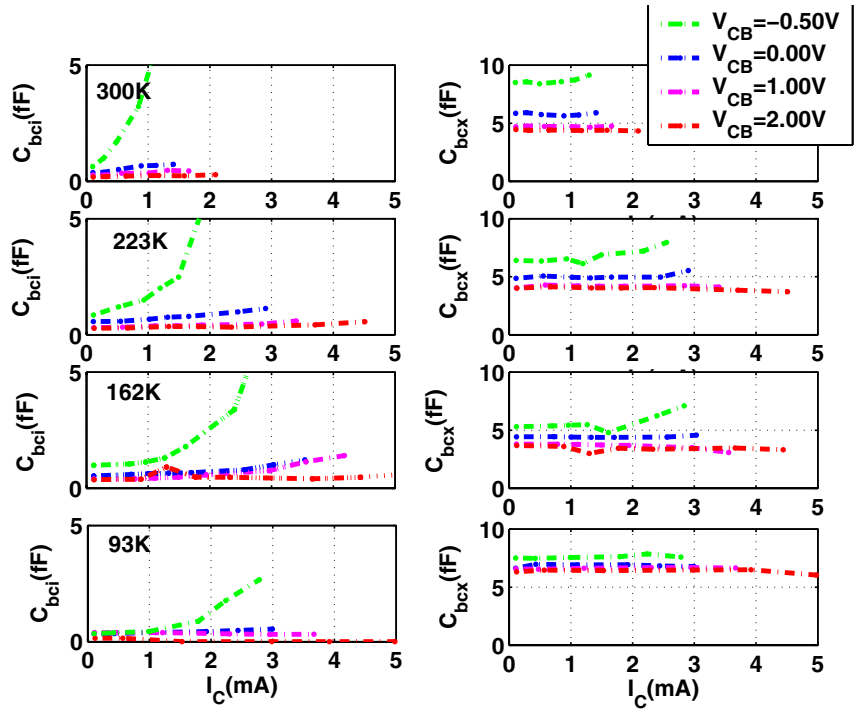

Figure 6.11: Extracted C_{bci}-I_C and C_{bcx}-I_C at 300, 223, 162 and 93 K.

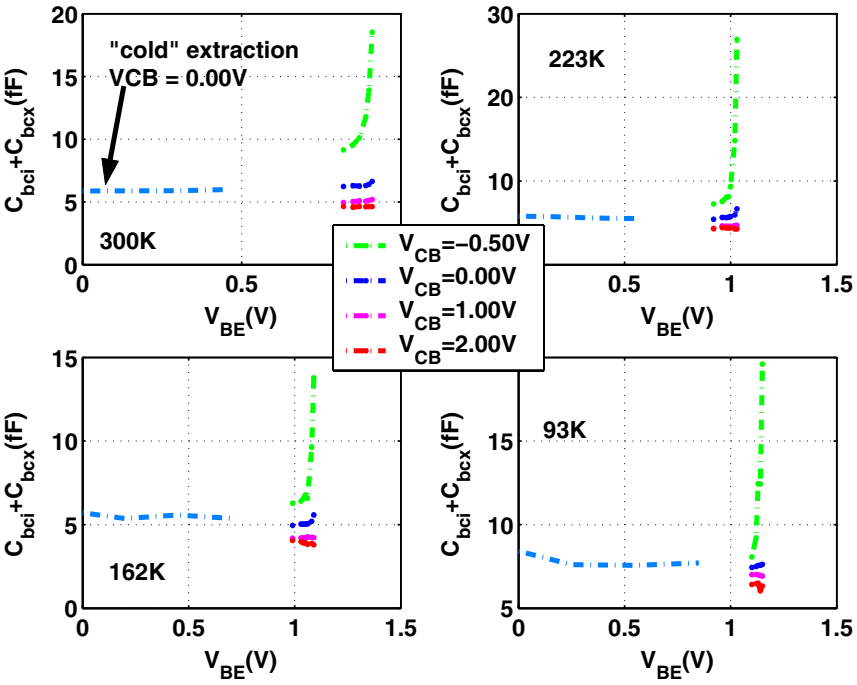

Figure 6.12: Extracted total $C_{BC}(C_{bci} + C_{bcx})$ vs V_{BE} from cold and hot extraction.

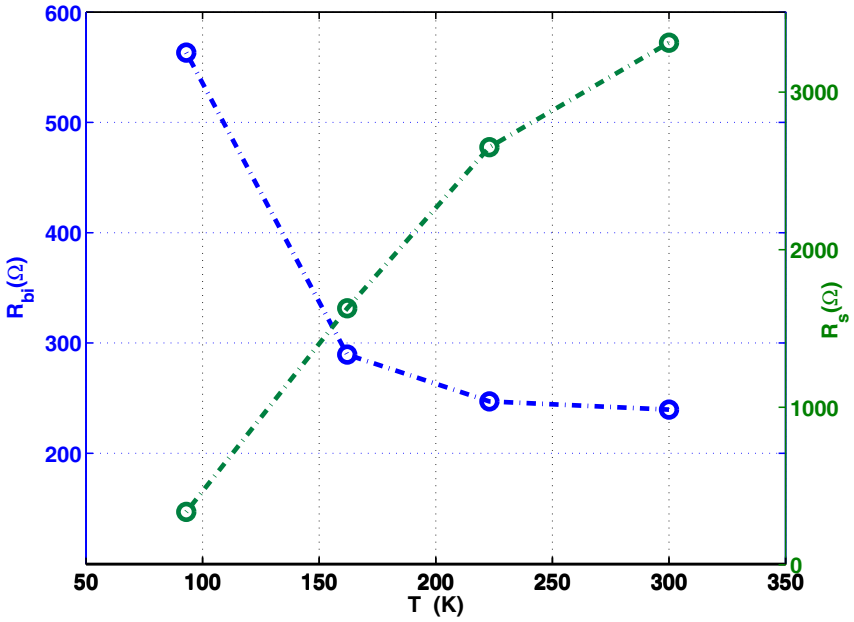

Figure 6.13: Extracted R_{bi} at $I_C = 1$ mA and R_s vs T.

scattering at lower temperature in the base and hence the mobility decrease and resistance increase. Carrier freezeout could also be responsible, as it is worse for higher doping as well.

The increase of R_{bi} with cooling can degrade noise figure; this, however, is offset by the decrease of thermal voltage and increase of f_T and current gain. The significant decrease of R_s will compromise the low RF loss advantage of a high resistivity (300 K) substrate, particularly for inductors and transmission lines. This increased substrate loss with cooling should be taken into consideration in cryogenic RF circuit design.

6.3 Substrate Network Implementation

The experience with small signal modeling showed that the substrate network is important for modeling the device high frequency behavior. So a substrate network is extended to Mextram Verilog-A code. To include distributive characteristics of low doping substrate, a substrate network is added between branches (C_1, S) and (C, S). Fig. 6.14 shows the substrate small signal equivalent circuit used in [37]. R_{sub} and C_{sub} are used to model distributive characteristics of substrate.

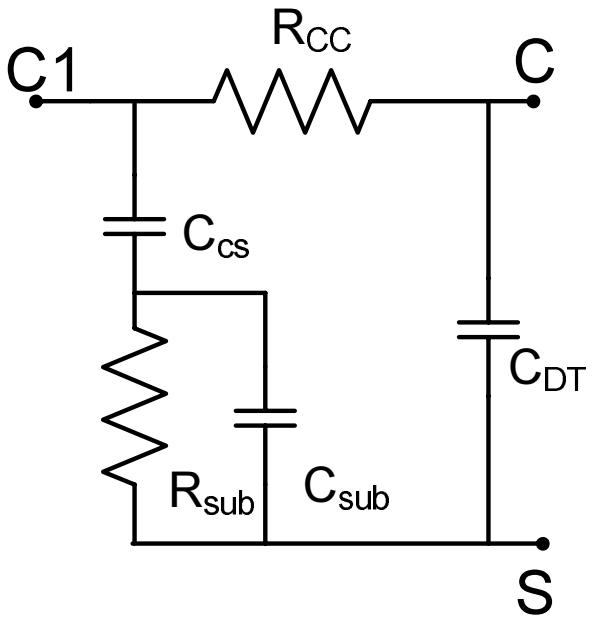

Figure 6.14: Small-signal equivalent circuit for substrate network.

C_{CS} is the CS junction capacitance. C_{DT} is physically the peripheral deep trench coupling capacitance between the N^+ buried layer and p-substrate equal to C_{CSO} in the small signal topology. In isothermal fitting of Y_{22}+Y_{12} from cold measurement, C_{SUB} and C_{DT} show very weak temperature dependence. Hence, C_{SUB} and C_{DT} can be fixed at the values extracted from reference temperature. The extracted R_{SUB} is consistent with measured substrate resistivity as shown in Fig. 6.15. Though it is not very consistent with the extraction from small signal, they share a similar temperature dependence.

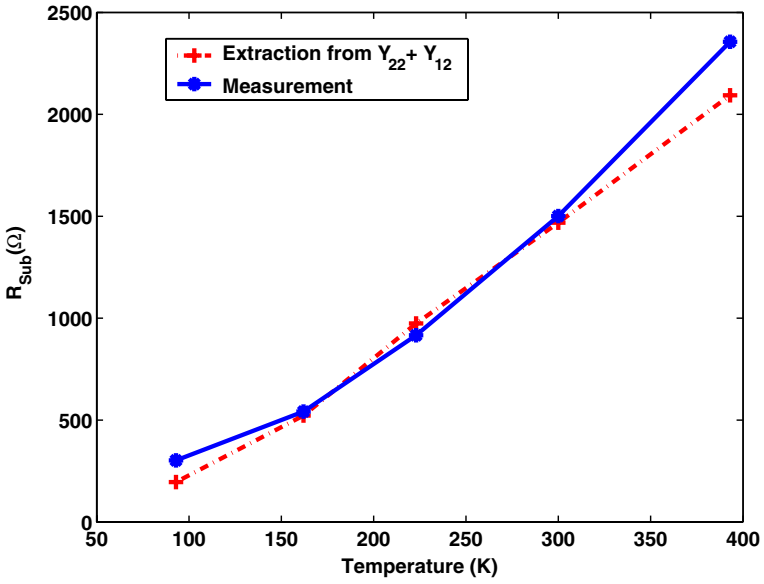

Figure 6.15: Small-signal equivalent circuit for substrate network.

CHAPTER 7

CONCLUSION

At low temperatures, the deviation of $I_C - V_{BE}$ slope from ideal $1/V_T$ is much larger than what can be modeled with q_B. Furthermore, below 100K, the T-dependence of $I_C - V_{BE}$ and $I_B - V_{BE}$ becomes increasingly weaker than predicted by Shockley theory. A N_F factor that increases with cooling has been used to model this deviation, such that the slope $1/(N_F V_T)$ does not increase as much as the ideal $1/V_T$. Based on a similar consideration, the T-dependence of N_F is included in the T-dependence model of I_S. The same strategy is both used for I_C and I_B, so current gain β_f is no longer necessary.

In this work, only the forward mode of operation has been discussed. Similar modification, however, has been made to model the reverse mode.

The temperature dependence of V_{BE} is also examined. The $\triangle V_{BE} - T$ is not linear at low temperature. This should be taken into account when designing bandgap reference.

$I_{B_{EN}}$ is added between B_2 and E_1 to account for forward bias trap-assisted tunneling current, which becomes important below 100K. Substrate network is included as part of the model, as shown in Fig. 7.1. The modifications and extensions based on Mextram is primarily to increase its applicable temperature range. Most of the modifications and extensions can be directly applied to other compact models as well. Verilog-A is used for model implementation, and IC-CAP is used for parameter extraction.

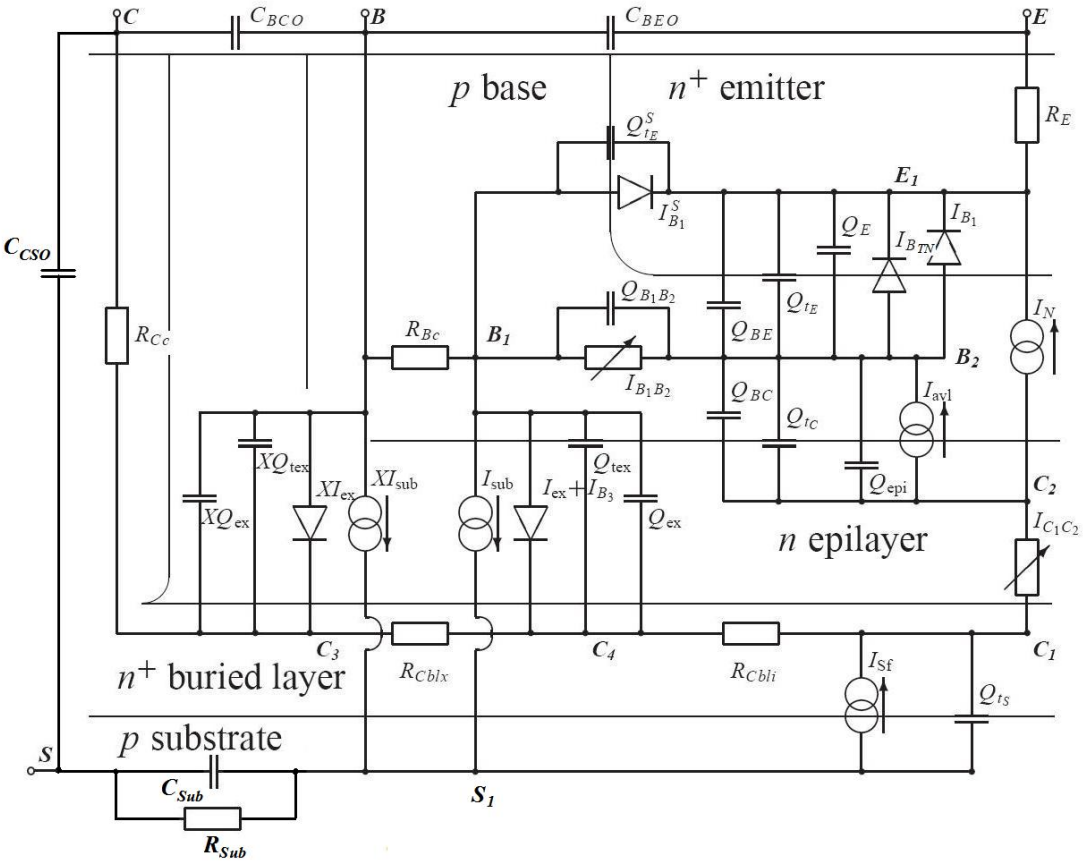

Figure 7.1: Modified equivalent circuit.

BIBLIOGRAPHY

[1] J. D. Cressler, "SiGe HBT BiCMOS technology for extreme environment applications," in *JPL Extreme Environment Workshop*, 2005.

[2] R. V. D. Toorn, J. C. J. Paasschens, and W. J. Kloosterman, *The Mextram Bipolar Transistor Model–Level 504.7*. Delft University of Technology, 2008.

[3] J. D. Cressler and G. Niu, *Silicon-Germanium Heterojunction Bipolar Transistor*. Artech House, 2002.

[4] F. Aniel, N. Zerounian, A. Gruhle, C. Mahner, G. Vernet, and R. Adde, "Temperature dependence of SiGe HBT static and dynamic characteristics," *J. Phys. IV France*, vol. 48, pp. 1776–1781, Aug. 2001.

[5] J. D. Cressler, "Using SiGe HBTs for extreme environment electronics," in *Dig. of IEEE BCTM*, pp. 248–251, 2005.

[6] D. B. M. Klaassen, "A unified mobility model for device simulation-I. model equations and concentration dependence," *IEEE Transactions of Electron Devices*, vol. 35, no. 7, pp. 953–959, 1992.

[7] L. Luo, G. Niu, K. Moen, and J. D. Cressler, "Compact modeling of the temperature dependence of parasitic resistances in SiGe HBTs down to 30 K," *IEEE Transactions on Electron Devices*, 2009, submitted.

[8] Z. Xu, G. Niu, L. Luo, P. S. Chakraborty, P. Cheng, D. Thomas, and J. D. Cressler, "Cryogenic rf small-signal modeling and parameter extraction of SiGe HBTs," in *Proc. of IEEE Topical Meeting on SiRF*, pp. 1–4, 2009.

[9] Z. Xu, X. Wei, G. Niu, L. Luo, D. Thomas, and J. D. Cressler, "Modeling of temperature dependent $I_C - V_{BE}$ characteristics of SiGe HBTs from 43-400 K," in *Proc. of IEEE BCTM*, pp. 81–84, 2008.

[10] B. J. Widlar, "New developments in IC voltage regulators," *IEEE Journal of Solid-State Circuits*, vol. 6, no. 1, pp. 2–7, 1971.

[11] J. D. Cressler, *Silicon Heterostructure handbook*. Taylor and Francis, 2006.

[12] H. C. Graaff and W. J. Kloosterman, *Compact Transistor Modeling for Circuit Design*. New York: Springer Verlag, 1990.

[13] J. C. J. Paasschens and W. J. Kloosterman, *The Mextram Bipolar Transistor Model–Level 504*. Nat Lab Unclassified Report, NL-UR 2000/811, Koninklijke Philips Electronics, 2000.

[14] D. Fitzpatrick and I. Miller, *Analog Behavioral Modeling with Verilog-A Language*. Kluwer Academic Publisher, 1999.

[15] H.-C. Wu, S. Mijalkovic, J. G. Macias, and J. Burghartz, "Mixed compact and behavior modeling using AHDL Verilog-A," in *Proceedings of the 2003 Behavoir Modeling and Simulaiton International Workshop*, pp. 139–143, 2003.

[16] *Agilent 85190A IC-CAP 2006 Reference*. Agilent Technologies, 2006.

[17] J. C. J. Paasschens, W. J. Kloosterman, and R. J. Havens, *Parameter Extraction for the Bipolar Transistor Model Mextram Level 504*. Nat Lab Unclassified Report, NL-UR 2001/801, Koninklijke Philips Electronics, 2001.

[18] H. K. Gummel and H. C. Poon, "An integral charge-control model for bipolar transistors," *Bell System Technical Journal*, vol. 49, pp. 827–852, 1970.

[19] C. C. McAndrew, J. A. Seitchik, D. F. Bowers, M. Dunn, M. Foisy, I. Getreu, M. McSwain, S. Moinian, J. Parker, D. J. Roulston, M. Schroter, P. van Wijnen, and L. F. Wagner, "VBIC95, the vertical bipolar inter-company model," *IEEE Journal of Solid-State Circuits*, vol. 31, no. 10, pp. 1476–1483, 1996.

[20] F. Pourchon, H. Beckrich-Ros, C. Raya, C. Faure, B. Gautheron, J. P. Blanc, B. Reynard, and D. Celi, "High accuracy temperature bipolar modeling for demanding bandgap application," in *Proc. of IEEE BCTM*, pp. 180–183, 2007.

[21] C. D. Thurmond, "The standard thermodynamic functions for the formation of electrons and holes in Ge, Si, GaAs, and GaP," *Journal of Electrochemical Society*, vol. 122, no. 8, pp. 1133–1141, 1975.

[22] Z. Feng, *Compact Modeling of SiGe HBTs Using Verilog-A*. Master Thesis, Auburn University, 2006.

[23] Z. Feng, G. Niu, C. Zhu, L. Najafizadeh, and J. D. Cressler, "Temperature scalable modeling of SiGe HBT DC current down to 43 K," *ECS Trans.*, vol. 3, pp. 927–936, 2006.

[24] S. L. Lin and C. A. T. Salama, "A V_{BE}(t) model with application to bandgap reference design," *IEEE Journal of Solid-State Circuits*, vol. 20, pp. 1283–1285, 1985.

[25] J. A. D. Alamo and R. M. Swanson, "Forward-bias tunneling: a limitation to bipolar device scalings," *IEEE Electron Devices Letters*, vol. 7, pp. 629–631, Nov 1986.

[26] S. H. Voldman, J. B. J. T. D. Linton, and S. L. Titcomb, "Unified generation model with donor- and acceptor-type trap states for heavily doped silicon," in *Dig. of IEDM Tech*, pp. 349–352, 1990.

[27] T. Y. Chen, J. Chen, P. K. Ko, and C. Hu, "The impact of gate-induced drain leakage current on MOSFET scaling," in *Dig. of IEDM Tech*, pp. 718–721, 1987.

[28] Y. Igura, H. Matsuoka, and E. Takeda, "New device degradation due to 'cold' carriers created by band-to-band tunneling," *IEEE Electron Device Letters*, vol. 10, no. 5, pp. 227–229, 1989.

[29] G. A. M. Hurkx, D. B. M. Klaassen, and M. P. G. Knuvers, "A new recombination model for device simulation including tunneling," *IEEE Transactions of Electron Devices*, vol. 39, no. 2, pp. 331–338, 1992.

[30] H.-C. Wu, *A scalable Mextram Model for Advanced Bipolar Circuit Design*. Ph.D. Thesis, Delft University of Technology, 2007.

[31] H. J. Gopen and A. Y. C. Yu, "h_{FE} falloff at low temperatures," *IEEE Transactions on Electron Devices*, no. 12, pp. 1146–1148, 1971.

[32] A. G. Chynoweth, W. L. Feldmann, and R. A. Logan, "Excess tunneling current in silicon esaki junctions," *Physical Review*, vol. 121, no. 3, pp. 684–694, 1960.

[33] J. Berkner, "Compact models for bipolar transistors," in *European IC-CAP Device Modeling Workshop*, March 2002.

[34] K. Lee, K. Choi, S.-H. Kook, D.-Y. Cho, K.-W. Park, and B. Kim, "Direct parameter extraction of SiGe HBTs for the VBIC bipolar compact model," *IEEE Transactions on Electron Devices*, vol. 52, no. 3, pp. 375–384, 2005.

[35] H.-Y. Chen, K.-M. Chen, G.-W. Huang, and C.-Y. Chang, "Small-signal modeling of SiGe HBTs using direct parameter-extraction method," *IEEE Transactions on Electron Devices*, vol. 53, no. 9, pp. 2287–2295, 2006.

[36] J.-S. Rieh, D. Greenberg, B. Jagannathan, G. Freeman, and S. Subbanna, "Measurement and modeling of thermal resistance of high speed SiGe heterojunction bipolar transistors," in *Proc. Silicon Monolithic Integrated Circuits in RF System*, pp. 110–113, 2001.

[37] U.Basaran and M. Berroth, "An accurate method to determine the substrate network elements and base resistance," in *Proc. of IEEE BCTM*, pp. 93–96, 2003.

APPENDICES

APPENDIX A

VERILOG-A CODE IMPLEMENTATION WITH KEY IMPROVED MODELS

A.1 Improved Ideality Factor Temperature Mapping

```
NF_T = NF*(1.0+(1-tN)*pow(ANF/tN,XNF));

NR_T = NR*(1.0+(1-tN)*pow(ANR/tN,XNR));

NEI_T = NEI*(1.0+(1-tN)*pow(ANE/tN,XNE));

NCI_T = NCI*(1.0+(1-tN)*pow(ANC/tN,XNC));
```

A.2 Improved Saturation Current Temperature Mapping

```
    tvgb = ‘EAA*‘EAB*tN*pow(Trk,2)/((‘EAB+Trk)*(‘EAB+Tk))
-‘EAA*‘EAB*pow(Trk,2)/pow((Trk+‘EAB),2);
```

VGB_T = VGBR+tvgb;

IS_T = IS*pow((pow(tN,XTI)*exp(-VGB_T*(1.0-tN)/Vt)),(1.0/NF_T));

ISR_T = IS*pow((pow(tN,XTI)*exp(-VGB_T*(1.0-tN)/Vt)),(1.0/NR_T));

$VGBE_T$ = VGBE+tvgb;

$IBEI_T$ = IBEI*pow((pow(tN,XTE)*exp(-$VGBE_T$*(1.0-tN)/Vt)),(1.0/NEI_T));

$VGBC_T$ = VGBC+tvgb;

$IBCI_T$ = IBCI*pow((pow(tN,XTC)*exp(-$VGBC_T$*(1.0-tN)/Vt)),(1.0/NCI_T));

$ISBETAT_T$ = ISBETAT*exp(K1*(-VGB_T*(1.0-tN)/Vt));

A.3 Modified Trasfer Current Model

```
If0 = 4.0 * IS_TM / IK_TM;

f1 = If0 * exp (( Vb2e1*VtINV) *(1/ NF_T));

n0 = f1 / (1.0 + sqrt(1.0 + f1));

f2 = 4.0 * ISR_TM / IKR_TM * exp (ln(eVb2c2star) *(1/ NR_T));

Ir = ISR_TM * exp (ln(eVb2c2star) *(1/ NR_T));

If = IS_TM * exp (( Vb2e1*VtINV) *(1/ NF_T));

In =( If-Ir) /qBI ;
```

A.4 Modified Base Current Model

```
    if (XREC == 0.0)
    Ib1 = (1.0 - XIBI) * IBEI_T * (exp (( Vb2e1*VtINV) *(1/ NEI_T)) - 1.0);
    else
    Ib1 = (1.0 - XIBI) * (1.0 - XREC) * IBEI_T * (exp (( Vb2e1*VtINV) *(1/ NEI_T))
- 1.0) + (1.0 - XIBI) * (1.0 + Vtc / VEF_T)* XREC * (IBEI_T * (exp (( Vb2e1*VtINV)
*(1/ NEI_T)) - 1.0) + IBEI_T * (exp ((ln(eVb2c2star)) *(1/ NCI_T)) - 1.0));


    Ib1s = XIBI * IBEI_T * (exp (( Vb1e1*VtINV) *(1/ NEI_T)) - 1.0);


    `expLin(tmpExp,Vb2e1 * VtINV / MLF)
    Ib2 = IBF_TM * (tmpExp - 1.0) + GMIN * Vb2e1;
    Ibetat = ISBETAT_TM*exp(Vb2e1/STN);
    `expLin(tmpExp,0.5 * Vb1c4 * VtINV)
    Ib3 = IBR_TM * (eVb1c4 - 1.0) / (tmpExp + exp(0.5 * VLR * VtINV)) + GMIN *
Vb1c4;


    g1 = If0 * eVb1c4;
    g1 = 4.0 * ISR_TM / IKEX_TM * exp (( Vb1c4*VtINV) *(1/ NCI_T));
    g2 = 4.0 * eVb1c4VDC;
    nBex = g1 / (1.0 + sqrt(1.0 + g1));
    pWex = g2 / (1.0 + sqrt(1.0 + g2));
    Iex = IBCI_T * (2*exp (( Vb1c4*VtINV) *(1/ NCI_T)) / (1.0 + sqrt(1.0 + g1))
- 1.0);
```